Dear Author,

Here are the proofs of your article.

- You can submit your corrections **online**, via **e-mail** or by **fax**.

- For **online** submission please insert your corrections in the online correction form. Always indicate the line number to which the correction refers.

- You can also insert your corrections in the proof PDF and **email** the annotated PDF.

- For fax submission, please ensure that your corrections are clearly legible. Use a fine black pen and write the correction in the margin, not too close to the edge of the page.

- Remember to note the **journal title**, **article number**, and **your name** when sending your response via e-mail or fax.

- **Check** the metadata sheet to make sure that the header information, especially author names and the corresponding affiliations are correctly shown.

- **Check** the questions that may have arisen during copy editing and insert your answers/ corrections.

- **Check** that the text is complete and that all figures, tables and their legends are included. Also check the accuracy of special characters, equations, and electronic supplementary material if applicable. If necessary refer to the *Edited manuscript*.

- The publication of inaccurate data such as dosages and units can have serious consequences. Please take particular care that all such details are correct.

- Please **do not** make changes that involve only matters of style. We have generally introduced forms that follow the journal's style.
  Substantial changes in content, e.g., new results, corrected values, title and authorship are not allowed without the approval of the responsible editor. In such a case, please contact the Editorial Office and return his/her consent together with the proof.

- If we do not receive your corrections **within 48 hours**, we will send you a reminder.

- Your article will be published **Online First** approximately one week after receipt of your corrected proofs. This is the **official first publication** citable with the DOI. **Further changes are, therefore, not possible.**

- The **printed version** will follow in a forthcoming issue.

Please note

After online publication, subscribers (personal/institutional) to this journal will have access to the complete article via the DOI using the URL: http://dx.doi.org/[DOI].
If you would like to know when your article has been published online, take advantage of our free alert service. For registration and further information go to: http://www.link.springer.com.

Due to the electronic nature of the procedure, the manuscript and the original figures will only be returned to you on special request. When you return your corrections, please inform us if you would like to have these documents returned.

Metadata of the article that will be visualized in OnlineFirst

ArticleTitle	Partial melting of secondary pyroxenite at 1 and 1.5 GPa, and its role in upwelling heterogeneous mantle
Article Sub-Title	
Article CopyRight	Springer-Verlag GmbH Germany (This will be the copyright line in the final PDF)
Journal Name	Contributions to Mineralogy and Petrology

Corresponding Author	Family Name	**Borghini**
	Particle	
	Given Name	**Giulio**
	Suffix	
	Division	Dipartimento di Scienze della Terra "Ardito Desio"
	Organization	Università degli Studi di Milano
	Address	Via Botticelli 23, 20133, Milan, Italy
	Phone	
	Fax	
	Email	giulio.borghini@unimi.it
	URL	
	ORCID	http://orcid.org/0000-0002-0246-7478
Author	Family Name	**Fumagalli**
	Particle	
	Given Name	**P.**
	Suffix	
	Division	Dipartimento di Scienze della Terra "Ardito Desio"
	Organization	Università degli Studi di Milano
	Address	Via Botticelli 23, 20133, Milan, Italy
	Phone	
	Fax	
	Email	
	URL	
	ORCID	
Author	Family Name	**Rampone**
	Particle	
	Given Name	**E.**
	Suffix	
	Division	
	Organization	DISTAV, Università di Genova
	Address	16132, Genoa, Italy
	Phone	
	Fax	
	Email	
	URL	

Abstract	We performed partial melting experiments at 1 and 1.5 GPa, and 1180–1400 °C, to investigate the melting under mantle conditions of an olivine-websterite (GV10), which represents a natural proxy of secondary (or stage 2) pyroxenite. Its subsolidus mineralogy consists of clinopyroxene, orthopyroxene, olivine and spinel (+garnet at 1.5 GPa). Solidus temperature is located between 1180 and 1200 °C at 1 GPa, and between 1230 and 1250 °C at 1.5 GPa. Orthopyroxene (±garnet), spinel and clinopyroxene are progressively consumed by melting reactions to produce olivine and melt. High coefficient of orthopyroxene in the melting reaction results in relatively high SiO_2 content of low melt fractions. After orthopyroxene exhaustion, melt composition is controlled by the composition of coexisting clinopyroxene. At increasing melt fraction, CaO content of melt increases, whereas Na_2O, Al_2O_3 and TiO_2 behave as incompatible elements. Low Na_2O contents reflect high partition coefficient of Na between clinopyroxene and melt ($D_{Na_2O}^{cpx/liquid}$). Melting of GV10 produces Quartz- to Hyperstene-normative basaltic melts that differ from peridotitic melts only in terms of lower Na_2O and higher CaO contents. We model the partial melting of mantle sources made of different mixing of secondary pyroxenite and fertile lherzolite in the context of adiabatic oceanic mantle upwelling. At low potential temperatures ($T_P < 1310$ °C), low-degree melt fractions from secondary pyroxenite react with surrounding peridotite producing orthopyroxene-rich reaction zones (or refertilized peridotite) and refractory clinopyroxene-rich residues. At higher T_P (1310–1430 °C), simultaneous melting of pyroxenite and peridotite produces mixed melts with major element compositions matching those of primitive MORBs. This reinforces the notion that secondary pyroxenite may be potential hidden components in MORB mantle source.

Keywords (separated by '-')	Pyroxenites - Experimental petrology - Partial melting - Basalt composition - Mantle heterogeneity - Melt productivity

CrossMark

ORIGINAL PAPER

Partial melting of secondary pyroxenite at 1 and 1.5 GPa, and its role in upwelling heterogeneous mantle

Giulio Borghini[1] · P. Fumagalli[1] · E. Rampone[2]

Abstract We performed partial melting experiments at 1 and 1.5 GPa, and 1180–1400 °C, to investigate the melting under mantle conditions of an olivine-websterite (GV10), which represents a natural proxy of secondary (or stage 2) pyroxenite. Its subsolidus mineralogy consists of clino-pyroxene, orthopyroxene, olivine and spinel (+garnet at 1.5 GPa). Solidus temperature is located between 1180 and 1200 °C at 1 GPa, and between 1230 and 1250 °C at 1.5 GPa. Orthopyroxene (±garnet), spinel and clinopyroxene are progressively consumed by melting reactions to produce olivine and melt. High coefficient of orthopyroxene in the melting reaction results in relatively high SiO_2 content of low melt fractions. After orthopyroxene exhaustion, melt composition is controlled by the composition of coexisting clinopyroxene. At increasing melt fraction, CaO content of melt increases, whereas Na_2O, Al_2O_3 and TiO_2 behave as incompatible elements. Low Na_2O contents reflect high partition coefficient of Na between clinopyroxene and melt ($D_{Na_2O}^{cpx/liquid}$). Melting of GV10 produces Quartz- to Hyperstene-normative basaltic melts that differ from peridotitic melts only in terms of lower Na_2O and higher CaO contents. We model the partial melting of mantle sources made of different mixing of secondary pyroxenite and fertile lherzolite in the context of adiabatic oceanic mantle upwelling. At low potential temperatures ($T_P < 1310$ °C), low-degree melt fractions from secondary pyroxenite react with surrounding peridotite producing orthopyroxene-rich reaction zones (or refertilized peridotite) and refractory clinopyroxene-rich residues. At higher T_P (1310–1430 °C), simultaneous melting of pyroxenite and peridotite produces mixed melts with major element compositions matching those of primitive MORBs. This reinforces the notion that secondary pyroxenite may be potential hidden components in MORB mantle source.

Introduction

Several geochemical and petrological observations support the idea that the source of oceanic basalts consists of heterogeneous mantle including peridotite mixed to pyroxene-rich olivine-poor mafic to ultramafic lithologies, such as eclogite and pyroxenite (e.g., Allègre and Turcotte 1986; Hirschmann and Stolper 1996; Kogiso et al. 2004a; Hofmann 2007; Sobolev et al. 2007; Lambart et al. 2013 and references therein). In particular, the contribution of pyroxene-rich lithologies has been invoked to explain the large isotopic and trace elements variability of oceanic basalts, although uncertainties still exist on how they affect their major element chemistry. Pyroxenites can either represent recycled crustal material or be introduced in the mantle by various magmatic processes, thus resulting in pyroxene-rich mantle components with a wide range of compositions

A5 ✉ Giulio Borghini
A6 giulio.borghini@unimi.it

A7 [1] Dipartimento di Scienze della Terra "Ardito Desio",
A8 Università degli Studi di Milano, Via Botticelli 23,
A9 20133 Milan, Italy

A10 [2] DISTAV, Università di Genova, 16132 Genoa, Italy

Ⓐ Springer

(e.g., Kogiso et al. 2004a; Herzberg 2011; Lambart et al. 2013).

A large number of experimental studies has been dedicated to partial melting of pyroxenites, and their phase relations and melting behavior, including solidus temperature and melt productivity, have been defined for a wide range of temperature, pressure and chemical compositions (e.g., Yaxley and Green 1998; Kogiso and Hirschmann 2001; Hirschmann et al. 2003; Pertermann and Hirschmann 2003a; Kogiso et al. 2004a; Keshav et al. 2004; Médard et al. 2006; Sobolev et al. 2007; Lambart et al. 2009a, 2013). Profiting of available experimental data, increasingly sophisticated geochemical models have investigated the role of mixed pyroxenite–peridotite mantle sources in the genesis of mid-ocean ridge basalts (MORBs) and ocean island basalts (OIBs) (e.g., Hirschmann and Stolper 1996; Phipps Morgan 2001; Sobolev et al. 2005, 2007; Stracke and Bourdon 2009; Herzberg 2006, 2011; Shortle and Maclennan 2011; Guerenko et al. 2013; Lambart et al. 2012, 2016; Shorttle et al. 2014; Delavault et al. 2015; Brown and Lesher 2016).

An important issue concerning the melting of pyroxenite-bearing mantle sources is the role of interaction between pyroxenite-derived melts and adjacent peridotite. Low-solidus mantle lithologies, such as crustal-derived rocks (eclogite or low-MgO pyroxenite), start to melt at higher pressure than "dry" peridotites (e.g., Yasuda et al. 1994; Pertermann and Hirschmann 2003a,b; Kogiso et al. 2004a; Kogiso and Hirschmann 2006; Yaxley and Sobolev 2007; Spandler et al. 2008). Their partial melts are expected to react to some extent with the surrounding subsolidus peridotite either modifying the composition of the rising melts (Pilet et al. 2008; Mallik and Dasgupta 2012, 2013, 2014), or creating new hybrid rock-types, called secondary or stage 2 pyroxenites (e.g., Yaxley and Green 1998; Sobolev et al. 2005, 2007; Herzberg 2006, 2011; Lambart et al. 2012). Moreover, heterogeneous upwelling mantle is subject to continuous events of partial melting and melt–rock reaction that potentially generate a large range of new lithological heterogeneities, including metasomatized peridotites and variably residual pyroxenites (e.g., Yaxley and Green 1998; Rosenthal et al. 2014). On this basis, recent models of basalts petrogenesis have proposed that secondary pyroxenites could represent diffuse mantle components in the MORB mantle sources (e.g., Sobolev et al. 2007; Lambart et al. 2012). Remarkably, such hybrid components are expected to produce MgO-rich partial melts that are able to percolate through peridotite with minimum interactions, thus preserving the pyroxenite signature of the original melts (Lambart et al. 2009a, 2012). These pyroxenites represent good candidates to transmit the trace element and isotopic signature of deep mantle heterogeneities without impacting the major element composition of basalts.

In spite of their inferred potential role in oceanic basalt generation, the origin of such hybrid mantle components, as well as the composition of their partial melts, is still not well defined, mostly due to the scarceness of available experimental data (Lambart et al. 2013). Lambart et al. (2012) investigated the interaction between melts produced by silica-deficient pyroxenites and peridotite, concluding that this process leads to the formation of secondary high-MgO pyroxenites, compositionally similar to those documented in the Ronda peridotite (Garrido and Bodinier 1999). Sobolev et al. (2007) investigated the melting behavior at 3.5 GPa of an olivine-free secondary pyroxenite originated by eclogite-derived silica-rich melts reacted with peridotite. However, experimental knowledge of the compositions of melts generated by secondary-type pyroxenites in the pressure range of basalt generation at mid-ocean ridges (i.e. 1–1.5 GPa; e.g., Presnall et al. 2002; Falloon et al. 2008) is currently not available.

Natural examples of secondary pyroxenites, originated by melt-peridotite reaction processes, have been documented in a number of studies on ultramafic massifs (i.e. Garrido and Bodinier 1999; Bodinier et al. 2008; Gysi et al. 2012; Marchesi et al. 2013; Borghini et al. 2013, 2016; Montanini and Tribuzio 2015). Specifically, pyroxenite layers in External Liguride (EL) mantle sequences (Northern Apennines, Italy) have been recently interpreted as the product of the reaction between deep infiltrated melts, likely derived from a hybrid eclogite-peridotite source, and the host peridotite (Borghini et al. 2016). Hence, they represent an excellent natural example of secondary (or stage 2) pyroxenite, which forms together with their host peridotite a potential source of E-MORBs (Borghini et al. 2013).

In this paper, we present the results of partial melting experiments performed on a selected natural olivine-websterite, whose origin by deep melt-rock reaction has been well supported on the basis of microstructural and geochemical observations (Borghini et al. 2013, 2016). The major aims of our work are to derive the extent and composition of melts produced by moderate to high degrees of melting of a secondary-type pyroxenite at 1 and 1.5 GPa and discuss the contribution of such melts to the composition of oceanic basalts.

Experimental and analytical techniques

Choice and preparation of starting material

The investigated bulk composition is an olivine websterite (sample GV10 of Borghini et al. 2016), representing a well-preserved cm-width pyroxenite layer from the External Liguride (EL) ophiolitic mantle sequences (Northern Apennines, Italy). Although the EL peridotites are considered

exposed subcontinental lithospheric mantle sectors (e.g., Rampone et al. 1995), their MORB-like isotopic composition and chemical features suggest that they were formed by lithospheric accretion of ordinary asthenospheric mantle (Rampone et al. 1995). Therefore, they represent good proxies of an MORB-type fertile mantle source that is modified by deep melt infiltration and melt–rock reaction processes before it undergoes partial melting and basaltic melt extraction (Borghini et al. 2013, 2016), as envisaged by recent MORB petrogenesis models (e.g., Lambart et al. 2012).

Olivine-websterite GV10 belongs to a group of pyroxenites having a geochemical signature inherited by a primary assemblage dominated by garnet and pyroxenes (mostly clinopyroxene and minor orthopyroxene). Originally, they represented clinopyroxene-rich garnet pyroxenites with orthopyroxene-rich borders against the host peridotite, indicative of an origin by silica-rich melt infiltration and crystallization within the peridotite at pressure >1.5 GPa (Borghini et al. 2016). Microstructural and geochemical observations on pyroxenite GV10 suggest that it was originated by deep melt-rock reaction, likely involving peridotite and a pyroxenite (or eclogite)-derived melt, thus supporting its secondary origin (Borghini et al. 2016). Moreover, the emplacement of these pyroxenite layers introduced short-length scale isotopic heterogeneity in the host peridotite, producing veined mantle domains with enriched Nd-isotopic signature that could represent a source of E-MORBs (Borghini et al. 2013). The selected sample GV10 thus constitutes an excellent analog of a secondary pyroxenite component in a fertile MORB mantle source.

Olivine-websterite GV10 has high X_{Mg} [molar Mg/$(Mg + Fe^{tot})$] (0.82–0.88) coupled with high CaO, moderate Al_2O_3 and low Na_2O contents (Fig. 1). Similar bulk compositions have been documented in Group C pyroxenites from Ronda (Spain; Garrido and Bodinier 1999) (Fig. 1). They have been inferred to result from interaction between peridotite and melts derived from garnet pyroxenites and have been recently interpreted as secondary pyroxenite (Lambart

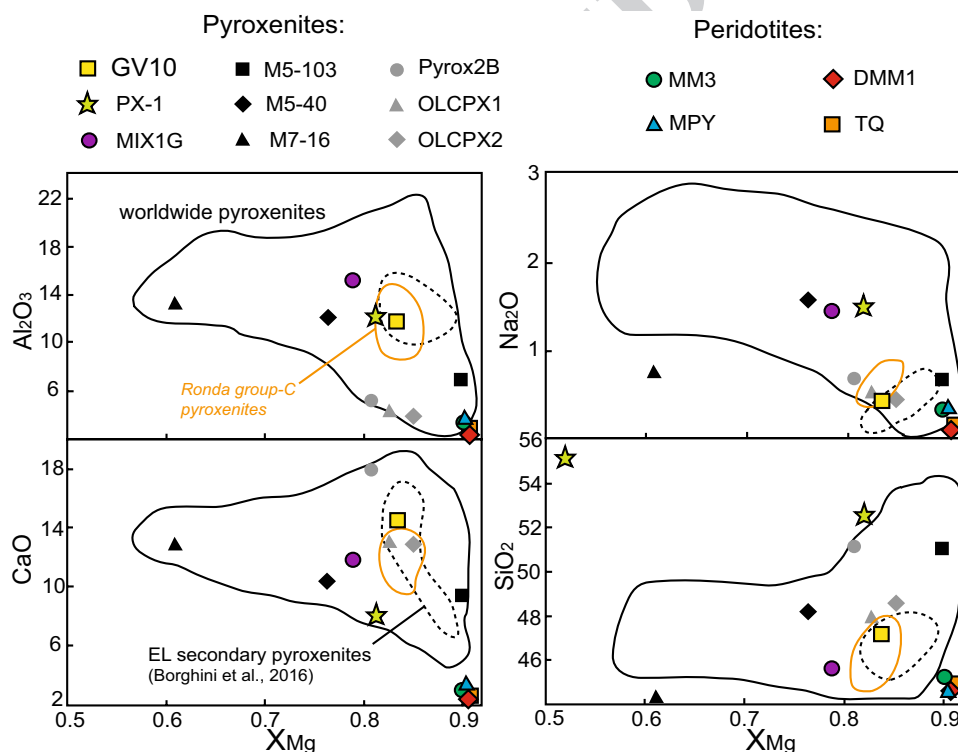**Fig. 1** X_{Mg} value vs. Al_2O_3, CaO, Na_2O and SiO_2 (wt%) diagrams showing the composition of the starting material used in this study (GV10), together with the composition of nominally "dry" pyroxenite and some peridotite bulks investigated in previous experimental studies at 1 and 1.5 GPa (see also Table 1). They are the silica-deficient pyroxenites M5-103, M5-40 and M7-16 studied by Lambart et al. (2009a); clinopyroxenites OLCPX1, OLCPX2 and Pyrox2B by Kogiso and Hirschmann (2001); garnet pyroxenite MIX1G (Hirschmann et al. 2003); lherzolite MM3 (Baker and Stolper 1994; Falloon et al. 2008); depleted lherzolite DMM1 (Wasylenki et al. 2003); MORB-pyrolite, MPY, and Tinaquillo lherzolite, TQ (Robinson et al. 1998). Purple star is the composition of the model secondary (silica-excess) pyroxenites experimentally investigated at 3.5 GPa by Sobolev et al. (2007). Also reported are the compositional fields of worldwide pyroxenites (*black line*) and External Liguride (EL) pyroxenites (*dotted line*) from Borghini et al. (2016), and group-C pyroxenites from Ronda (*orange line*) from Garrido and Bodinier (1999)

et al. 2012). Compared to bulk compositions of nominally "dry" pyroxenites previously investigated at 1 and 1.5 GPa, GV10 has higher CaO and lower Na_2O contents with respect to pyroxenites investigated by Lambart et al. (2009a) (Table 1; Fig. 1), and higher Al_2O_3 and slightly lower SiO_2 than clinopyroxenites studied by Kogiso and Hirschmann (2001) at 1.0 GPa (Table 1; Fig. 1). In spite of similar X_{Mg}, GV10 significantly differs in composition from model secondary pyroxenite PX-1 studied by Sobolev et al. (2007), for much higher CaO and lower SiO_2 and Na_2O contents (Fig. 1). Such difference in bulk rock composition suggests that pyroxenite GV10 did not simply originate by eclogite melt–peridotite reaction (as for model secondary pyroxenite PX-1, Sobolev et al. 2005), but more presumably resulted by interaction between a melt produced by an eclogite-peridotite mixed source (e.g., Mallik and Dasgupta 2012) and a peridotite, as argued by Borghini et al. (2016).

Pyroxenite GV10 has been crushed in an agate mortar, and pulverized to 2–4 μm using an agate-micronizing mill. Two pellets obtained pressing about 0.5 g of rock powder each have been wrapped in platinum foils, previously preconditioned for Fe, and mounted at the end of a shaft in a vertical furnace. A first Fe preconditioning of platinum foil was performed at 1500 °C for about 12 h at FMQ fO_2 conditions, by covering it with GV10 rock powder. Glass GV10 was obtained by heating the pellets up to 1500 °C at FMQ fO_2 conditions through a night and quenched in dry ice. Electron microprobe analysis on the GV10 glass indicated its homogeneous composition and the lack of any residual mineral phase. Fe loss was lower than 4% with respect to the starting rock powder composition (Table 1).

Experimental and analytical techniques

Experiments were conducted at 1.0 and 1.5 GPa, and temperatures from 1180 to 1400 °C, at the Laboratorio di Petrologia Sperimentale, Dipartimento di Scienze della Terra, University of Milano. Experiments at 1 GPa were carried out in a single-stage piston cylinder and experiments at 1.5 GPa in end-loaded piston cylinder using MgO-Pyrex-Salt assemblies. Run lasted from 50 to 240 h (Table 2). As we did not perform time series experiments, run durations of this work have been chosen following previous experiments on pyroxenite melting (i.e. Kogiso and Hirschmann 2001; Pertermann and Hirschmann 2003a, b). Accordingly, we performed super-solidus experiments with run durations ranging from 50 to 155 h. Subsolidus experiments lasted up to 240 h, in order to approach equilibrium of the run products and favor the development of textures with grain size suitable for microprobe analyses (Table 2).

Approximately, 20 mg of starting material was loaded into a graphite inner capsule (outer diameter 2.8 mm), and then welded into an outer Pt capsule (outer diameter 3.0 mm, length about 7–8 mm). Graphite is used to isolate the sample from the Pt capsule and avoid Fe-loss (e.g.,

Table 1 Starting compositions experimentally investigated at 1 and 1.5 GPa

	GV10	GV10	Lambart et al. (2009)			Kogiso and Hirschmann (2001)			B&S (1994)
	rock an.(*)	glass	M5-103	M5-40	M7-16	Pyrox2B	OLCPX1	OLCPX2	MM3
SiO_2	47.54	47.57 (12)	51.64	48.53	43.58	51.56	47.92	48.73	45.50
TiO_2	0.45	0.45 (6)	0.09	0.52	0.75	0.54	0.47	0.39	0.11
Al_2O_3	10.27	10.39 (6)	7.17	12.37	13.73	5.58	4.49	4.13	3.98
Cr_2O_3	0.16	0.15 (4)	0.60	0.12	0.07	0.00	0.00	0.00	0.68
FeO	7.23	6.99 (11)	4.97	9.02	14.51	7.01	9.26	7.93	7.18
MnO	0.17	0.18 (6)	0.10	0.20	0.30	0.10	0.13	0.12	0.13
MgO	19.15	19.23 (14)	24.57	16.64	12.52	16.19	23.38	24.42	38.30
CaO	14.43	14.49 (9)	10.13	10.89	13.77	18.18	13.72	13.71	3.57
Na_2O	0.50	0.48 (2)	0.71	1.65	0.75	0.84	0.63	0.57	0.31
K_2O	0.10	0.08 (2)	0.02	0.06	0.03	0.00	0.00	0.00	0.23
Total	100.00	100.00	100.00	100.00	100.00	100.00	100.00	100.00	100.00
X_{Mg}	0.82	0.83	0.90	0.77	0.61	0.81	0.82	0.85	0.09
CIPW[b]	0/27/4/37/31	0/27/5/37/30	2/32/0/28/36	0/28/8/22/41	0/18/31/27/22	0/12/5/63/19	0/37/0/47/15	0/35/4/47/14	0/63/16/7/13

All compositions are normalized to a sum of 100%. In the second column, in parentheses we report the errors (1σ) given in terms of least unit

Cited; e.g., 47.57 (12) and 0.45 (6) represent 47.57 ± 0.12 and 0.45 ± 0.06, respectively. $X_{Mg} = Mg/(Mg + Fe^{tot})$

B&S (1994) refers to Baker and Stolper (1994)

[a] Major element analyses by lithium metaborate/tetraborate fusion ICP on powder samples GV10 (Borghini et al. 2016)

[b] Normative composition in terms of Nepheline/Olivine/Hypersthene/Diopside/Feldspars

Table 2 Summary of experimental conditions and run products

Run	T (°C)	Time (h)	Phase assemblages and modes (wt%)						R2[a]	Fe loss (%)	Kd1	Kd2
			Olivine	cpx	opx	Spinel	Garnet	Glass				
Experiments at 1 GPa												
GV10-83-4	1180	240	5.2 (29)	74.4 (27)	16.1 (51)	4.5 (13)	0	0	0.1123	–	–	–
GV10-83-1	1200	120	6.6 (26)	78.9 (24)	7.3 (43)	5.4 (8)	0	1.8 (29)	0.1045	0.52	0.22	0.33
GV10-83-2	1250	96	10.5 (17)	72.2 (64)	0	4.5 (9)	0	12.6 (56)	0.1326	1.12	0.31	0.33
GV10-83-14	1280	83	12.1 (25)	45.4 (28)	0	2.2 (12)	0	40.2 (31)	0.0998	0.68	0.33	0.32
GV10-83-6	1300	95	13.2 (11)	29.7 (44)	0	0	0	56.7 (46)	0.1604	0.62	0.32	0.31
GV10-83-8	1330	146	8.6 (57)	0	0	0	0	91.3 (45)	0.1142	1.23	0.32	0.31
Experiments at 1.5 GPa												
GV10-83-16	1230	124	6.3 (21)	78 (41)	6.7 (53)	3.1 (19)	5.2 (46)	0	0.3421	–	–	–
GV10-83-9	1250	155	10.1 (35)	76.9 (36)	1.5 (38)	4.5 (28)	0	7.1 (38)	0.2046	0.05	0.31	0.34
GV10-83-10	1280	72	10.3 (35)	73.4 (58)	0	3.6 (11)	0	12.6 (53)	0.1899	0.24	0.31	0.33
GV10-83-13	1300	70	10.5 (32)	67.4 (55)	0	2.4 (13)	0	19.4 (44)	0.4765	1.89	0.30	0.33
GV10-83-18	1330	76	10.5 (17)	56.7 (33)	0	1 (9)	0	31.1 (37)	0.5624	2.33	0.30	0.32
GV10-83-15	1350	66	10.9 (21)	44.7 (57)	0	1.3 (11)	0	42.3 (62)	0.5471	0.82	0.33	0.32
GV10-83-21	1370	52	9.9 (11)	37.3 (41)	0	0	0	52.1 (35)	0.6333	0.56	0.33	0.32
GV10-83-22	1400	50	11.6 (8)	0	0	0	0	88.4 (22)	0.1944	0.77	0.34	0.32

Kd is the exchange coefficient of Fe^{2+} and Mg between olivine and liquid measured (1) and calculated (2) following Toplis (2005)

cpx clinopyroxene, *opx* orthopyroxene

[a] Sum of squared residuals in mass balance calculations. Numbers in parentheses are propagated errors from Monte Carlo simulations, given in terms of the least unit cited; e.g., 5.2 (29) and 74.4 (27) represent 5.2 ± 2.9 and 74.4 ± 2.7, respectively

Kinzler 1997; Walter 1998). Furthermore, the graphite-Pt assembly keeps the oxygen fugacity below the graphite–C–O vapor buffer (e.g., Ulmer and Luth 1991; Médard et al. 2008). We added a layer of vitreous carbon spheres (80–125 µm diameter) at the top of the capsule to enhance the storage and segregation of melt (e.g., Pickering-Witter and Johnson 2000; Wasylenki et al. 2003; Médard et al. 2006). Carbon spheres may also absorb water if present in the charge (Robinson et al. 1998). The mass of the vitreous spheres layer never exceeded 15% of the starting glass. To maintain anhydrous conditions, the platinum-graphite capsule loaded with the starting material was dried overnight in an oven at 250 °C before being rapidly welded shut. The thermocouple tip was separated from the platinum capsule by a 0.5-mm thick hard corundum disc. Assemblies were kept in oven at about 200 °C for several hours before running the experiments. Temperature was measured by K-type and S-type thermocouples and is considered to be accurate to ± 5 °C. An initial pressure of 0.25 GPa was applied, then the sample was first heated to 400 °C for 10 min in order to soften the Pyrex; pressure was raised to the experimental value before reaching the desired temperature. Runs were terminated by turning off the power. Capsules were enclosed in epoxy, sectioned lengthwise, polished and carbon-coated.

Run products were inspected by back-scattered electron images (BSE) and microanalyses were performed using a JEOL JXA 8200 Superprobe equipped with five WDS-wavelength-dispersive spectrometers and one energy dispersive spectrometer (EDS) at the Dipartimento di Scienze della Terra, University of Milano. Both images and X-ray element maps were extremely useful in textural examination of the experimental charges. Analyses on mineral phases were performed using 1 µm beam size and beam conditions of 15 kV and 5 nA. Counting time was 30 s for peak and 10 s for background. Whenever possible, in order to prevent alkali loss, we analyzed glass using a beam size of 5 µm, or 2–3 µm in thin interstitial films in experiments with very low melt fractions.

Results

Approach to equilibrium

The approach to equilibrium in experiments of this study is assessed by a number of observations, first of all the growth of compositionally homogeneous chemically unzoned minerals, as revealed by X-ray element maps (Supplementary Figure 1). A solid proof of approach to equilibrium is the systematic and consistent variations in mineral chemistry at different pressure and temperature conditions, as well as coherent element partitioning (see below). Phase abundances have been calculated by mass balance between the

	Journal : **Large 410**	Dispatch : **3-7-2017**	Pages : **24**
	Article No : **1387**	☐ LE	☐ TYPESET
	MS Code : **CTMP-D-17-00017**	☑ CP	☑ DISK

303 composition of coexisting phases and the bulk composition,
304 using a weighted least squares method (Table 2). Residual
305 sums of squares ranging from 0.09 and 0.63 are perfectly
306 comparable to other experimental studies (i.e. Kogiso and
307 Hirschmann 2001; Pertermann and Hirschmann 2003a, b;
308 Lambart et al. 2009a). Moreover, results of mass balance
309 calculations indicate that Fe loss, possibly due to fractures
310 in graphite inner capsule to the Pt outer capsule, was negli-
311 gible in these experiments (Table 2).

312   As a further test, we applied the method proposed by
313 Toplis (2005). The values of distribution coefficient K_D
314 between olivine and liquid measured in our experiments
315 differ from those computed using thermodynamic calcu-
316 lation (Toplis 2005) within the range of ± 0.02 (Table 2),
317 thus supporting the attainment of equilibrium. As only
318 exception, run GV10-83-1 at very low degree of melting
319 ($F = 1.8\%$, see below) yielded an olivine/liquid Kd_{Fe-Mg}
320 measured value much lower than the calculated one. On
321 this experiment, we did not adopt specific technique to
322 account for the effect of quench crystal growth on the very
323 small spots of melt, as applied in previous dedicated stud-
324 ies (i.e. Hirose and Kushiro 1993; Wasylenki et al. 2003;
325 Laporte et al. 2004; Dasgupta and Hirschmann 2007; Fal-
326 loon et al. 2008). Accordingly, the composition of glasses
327 produced at very low melting degrees ($F < 5\%$) in our
328 experiments must be considered with caution.

Phase assemblages and textures

330 Run products are summarized in Table 2, together with
331 experimental details.
332   Crystal size ranges from 1 to 10 μm in subsolidus exper-
333 iments and increases with increasing temperature, around
334 5–15 μm in experiments with low melt fractions (<20
335 wt%), and up to 80 μm in near-liquidus runs.
336   At 1 GPa and 1180 °C, the stable mineral assemblage is
337 made of prismatic grains of clinopyroxene, and orthopyrox-
338 ene (5–10 μm in size), minor rounded olivine and tiny spi-
339 nel (mostly 2–5 μm in size). At 1200 °C, few tiny interstitial
340 patches of glass coexist with clinopyroxene, orthopyroxene,
341 olivine and spinel. At 1250 °C, orthopyroxene is absent; resid-
342 ual clinopyroxene and olivine reach 15 μm in size (Fig. 2a),
343 and interstitial glass blebs (mostly confined at the top of the
344 capsule) are larger as compared to lower temperature experi-
345 ment. At 1280 °C, glass is still in equilibrium with clinopy-
346 roxene, olivine and spinel and it occurs as large pools (about
347 120–150 μm) at the rim of the capsule. At 1300 °C, spinel is
348 absent and a homogeneous glass coexists with coarse residual
349 clinopyroxene and olivine (10–30 μm). At 1330 °C, olivine
350 is the only residual phase and it consists of coarse polygonal
351 grains confined at the bottom portion of the capsule (Fig. 2b).
352   In experiments at 1.5 GPa, a subsolidus fine-grained
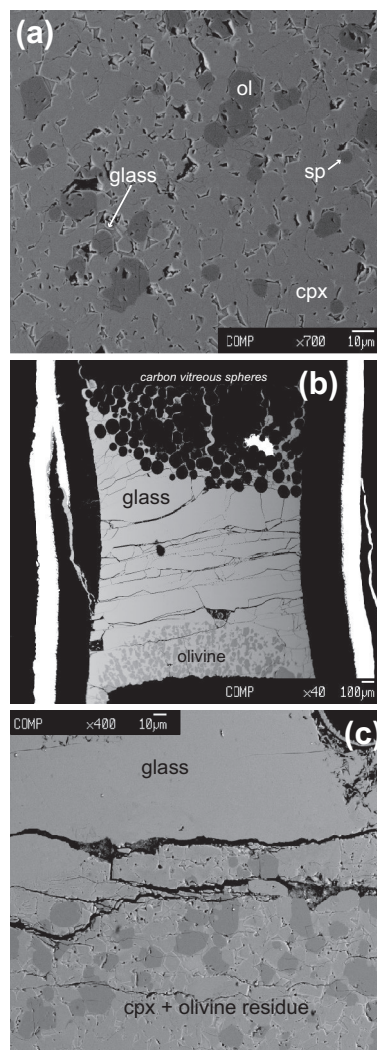353 (>10 μm) mineral assemblage made of clinopyroxene,

Fig. 2 Representative textures in melting experiments on pyroxen-ite GV10. **a** Back-scattered electron (BSE) image of melting experi-ment GV10-83-2 (1 GPa; 1250 °C): glass is mostly confined at the top of the capsule and occurs as interstitial blebs between residual clinopyroxene and olivine (around 15 μm in size) and smaller spi-nel (up to 5 μm). **b** BSE image of run GV10-83-8 (1 GPa; 1330 °C): residual olivine as coarse polygonal grains floating in the glass at the bottom of the capsule. **c** BSE image of experiment GV10-83-21 (1.5 GPa; 1370 °C): coarse clinopyroxene and olivine coexist with glass is either contained in the trap layer or as a pool towards the top of capsule

354 olivine, orthopyroxene, spinel and garnet is stable at
355 1230 °C. Garnet is the first phase to disappear at 1250 °C,
356 and orthopyroxene is no more present at 1280 °C. In runs
357 at temperatures from 1280 to 1350 °C, glass proportion
358 increases progressively with temperature and the residual
359 phases are clinopyroxene, olivine and spinel (Table 2).
360 Grain size is almost constant with clinopyroxene and oli-
361 vine ranging 10–30 μm and spinel always smaller than
362 5 μm. At 1370 °C, spinel is entirely consumed and coarse
363 clinopyroxene and olivine coexist with glass; in such

experiments with high degrees of melting, glass is either contained in the trap layer or as a pool towards the top of the capsule (Fig. 2c). At 1400 °C, rounded large olivines float in a homogeneous glass, thus indicating that olivine is the liquidus phase also at 1.5 GPa.

Liquid compositions as a function of pressure and temperature

AQ3 The glass compositions are reported in Table 3 and in Fig. 3, where major and minor element contents are plotted against melt fraction. Melt compositions are basaltic and vary significantly as a function of melt fraction (F) and only slightly with pressure.

At increasing melt fraction, MgO and CaO abundances progressively increase and Al_2O_3, Na_2O and TiO_2 contents decrease at both 1 and 1.5 GPa (Fig. 3). Na_2O and TiO_2 contents are lower than about 2 wt% in all experiments, and they decrease at increasing melt fraction at both pressures (Fig. 3). K_2O behaves as highly incompatible element, reaching about 0.4 wt% in experiments with the lowest melt fractions at 1 and 1.5 GPa, and drastically decreasing at increasing melting degree (Table 3).

The highest SiO_2 contents are observed in the experiments with the lowest melt fraction ($F < 8\%$); SiO_2 abundance significantly decreases as long as orthopyroxene is a melting phase and it remains almost constant once orthopyroxene is exhausted, i.e. at $F = 2–12\%$ at 1 GPa and $F > 7\%$ at 1.5 GPa. The FeO compositional trend is rather flat at 1 GPa, ranging from 7.1 to 8.3 wt%; at 1.5 GPa it has a convex shape, increasing up to 9.7 wt% with orthopyroxene consumption (corresponding to 20% melt fraction), and slightly decreasing after orthopyroxene disappearance at higher melt fraction (Fig. 3). Cr_2O_3 melt contents are very low as long as spinel is present as residual mineral, and increases at high melt fraction ($F > 60\%$) after spinel exhaustion, at both 1 and 1.5 GPa (Fig. 3). The X_{Mg} value $[X_{Mg} = Mg/(Mg + Fe_{tot})]$ of melts increases with the melt fraction, from 0.53 to 0.79 in runs at 1 GPa, and from 0.63 to 0.80 at 1.5 GPa (Table 3). It is positively correlated with X_{Mg} value of olivine and clinopyroxene (Fig. 4), supporting approach to equilibrium.

Differences in melt composition as a function of pressure are generally modest, except for higher SiO_2 and CaO abundances in experiments at 1 GPa with respect to those at 1.5 GPa (Supplementary Fiure 2).

In Fig. 5, the compositions of melts produced by GV10 pyroxenite are projected from diopside (Di) in the pseudo-ternary diagram forsterite (Fo)–Ca-Tschermak's pyroxene (CaTs)–quartz (Qz), together with the compositions of partial melts obtained in previous pyroxenite melting experiments at 1–1.5 GPa (Kogiso and Hirschmann 2001; Lambart et al. 2009). Lambart et al. (2009) demonstrated that the majority of melts produced by partial melting of silica-deficient pyroxenites plot on the right side of the CaTs-En join (Fig. 5), thus attesting the absence of a thermal divide at $P < 2$ GPa. Partial melts from GV10 pyroxenite, which is silica-deficient too, also plot on the right side of the CaTs-En join (Fig. 5), further supporting that the thermal divide is not relevant at such low pressures (1–1.5 GPa).

Mineral compositions as a function of pressure and temperature

Average compositions of minerals from each experimental run are listed in Table 3.

X_{Mg} value of olivine is 0.83 in the subsolidus runs at 1 and 1.5 GPa, and it increases with increasing degree of melting up to 0.92 (Table 3; Fig. 4). CaO content in olivine is rather high, spanning 0.3–0.5 wt% at both 1 and 1.5 GPa (Table 3), and it is comparable to previous experimental studies (e.g., Libourel 1999; Kogiso and Hirschmann 2001).

Clinopyroxene at subsolidus conditions has X_{Mg} values equal to 0.84, and rather high Na content (recalculated on the basis of 6 oxygens and all Fe = Fe^2; Na = 0.046 and 0.052 a.p.f.u. at 1 and 1.5 GPa, respectively), suggesting an increase of the jadeitic component with pressure (Table 3). At increasing melt fraction, residual clinopyroxene shows progressively higher X_{Mg} values, ranging from 0.84 to 0.9 (Fig. 4), and systematically lower jadeite (from about 5 to 1%) and TiO_2 concentrations, at both 1 and 1.5 GPa (Table 3). The Al_2O_3 content does not vary significantly along the melting interval, but it tends to be higher in residual clinopyroxene of melting experiments at 1.5 GPa (Table 3). The CaO abundance tends to increase with melt fraction in experiments at 1 GPa, whereas it remains rather constant at 1.5 GPa (Table 3). The Cr_2O_3 content slightly increases at higher melt fraction (Table 3).

Spinels are Al-rich and have X_{Mg} (0.68–0.77 at 1 GPa, 0.66–0.82 at 1.5 GPa) and X_{Cr} (0.021–0.036 at 1 GPa, 0.019–0.038 at 1.5 GPa) that increase with melt fraction. Their TiO_2 content stays low at both 1 and 1.5 GPa ($TiO_2 \leq 0.26$ wt%) without any correlation with pressure or melt fraction (Table 3).

Orthopyroxenes have X_{Mg} ranging 0.84–0.85, and Al_2O_3 contents around 7–8 wt% in subsolidus runs, as well as in near-solidus experiments. The CaO contents are rather high, with values from 1.9 to 2.1 wt% at 1 GPa and from 1.8 to 2.1 wt% at 1.5 GPa (Table 3).

Average composition of garnet in subsolidus experiments at 1.5 GPa and 1230 °C consists of 0.62 pyrope, 0.20 almandine, 0.14 grossular molar fractions, and it shows very low Cr_2O_3, TiO_2, Na_2O contents (Table 3).

Table 3 Average compositions (wt%) of liquids and residual phases

Run	Phase	SiO_2		TiO_2		Al_2O_3		Cr_2O_3		FeO		MgO	
Exp. at 1 GPa													
GV10-83-4	ol (10)	39.75	(51)	0.03	(2)	0.13	(8)	0.04	(3)	15.60	(26)	43.95	(55)
$F = 0$	cpx (15)	49.98	(89)	0.34	(23)	8.79	(124)	0.12	(4)	5.47	(28)	15.91	(41)
	opx (9)	51.55	(77)	0.21	(5)	8.02	(54)	0.14	(3)	9.47	(32)	28.16	(25)
	sp (10)	0.34	(13)	0.17	(5)	63.34	(85)	2.11	(17)	15.05	(43)	17.78	(55)
GV10-83-1	gl (11)	50.92	(39)	1.98	(14)	19.66	(45)	0.02	(1)	7.99	(32)	5.03	(18)
$F = 0.02$	ol (18)	40.39	(28)	0.03	(2)	0.22	(21)	0.03	(2)	15.51	(26)	44.15	(46)
	cpx (17)	50.81	(55)	0.49	(6)	7.99	(47)	0.14	(3)	5.62	(19)	16.89	(28)
	opx (16)	53.01	(90)	0.22	(4)	7.19	(110)	0.13	(3)	9.27	(19)	28.39	(39)
	sp (4)	0.25	(9)	0.16	(5)	63.42	(7)	2.24	(14)	15.36	(39)	18.21	(41)
GV10-83-2	gl (12)	50.53	(37)	1.29	(19)	16.37	(30)	0.05	(2)	8.03	(23)	8.90	(20)
$F = 0.13$	ol (17)	40.69	(20)	0.02	(3)	0.11	(6)	0.04	(3)	13.05	(57)	46.21	(43)
	cpx (18)	51.19	(31)	0.42	(6)	7.83	(45)	0.17	(3)	5.24	(30)	17.47	(55)
	sp (10)	0.33	(14)	0.21	(5)	64.87	(147)	2.84	(37)	12.67	(113)	19.14	(56)
GV10-83-14	gl (8)	48.36	(14)	0.76	(5)	14.50	(16)	0.06	(2)	8.31	(10)	12.43	(8)
$F = 0.40$	ol (8)	40.72	(16)	0.05	(2)	0.14	(8)	0.05	(1)	10.63	(7)	48.01	(7)
	cpx (12)	50.85	(34)	0.31	(3)	7.26	(29)	0.17	(2)	4.26	(9)	17.91	(14)
	sp (5)	0.36	(7)	0.21	(3)	63.63	(40)	3.56	(30)	11.06	(19)	20.43	(38)
GV10-83-6	gl (13)	47.42	(59)	0.71	(5)	13.99	(76)	0.07	(2)	7.87	(11)	13.38	(57)
$F = 0.57$	ol (12)	40.90	(18)	0.02	(2)	0.10	(4)	0.06	(4)	9.37	(20)	49.13	(21)
	cpx (16)	50.96	(80)	0.26	(7)	7.30	(117)	0.36	(8)	3.61	(15)	17.47	(60)
GV10-83-8	gl (15)	47.96	(66)	0.48	(8)	11.54	(58)	0.18	(3)	7.11	(37)	15.23	(33)
$F = 0.91$	ol (11)	41.47	(14)	0.03	(1)	0.06	(3)	0.09	(4)	7.51	(25)	50.67	(19)
Exp. at 1.5 GPa													
GV10-83-16	ol (6)	39.48	(13)	0.02	(2)	0.10	(4)	0.05	(3)	15.60	(23)	43.90	(32)
$F = 0$	cpx (13)	50.48	(32)	0.50	(8)	8.43	(42)	0.12	(4)	5.65	(16)	17.11	(21)
	opx (9)	52.33	(69)	0.28	(17)	7.19	(91)	0.08	(6)	9.23	(14)	28.82	(40)
	sp (4)	0.27	(13)	0.16	(2)	63.20	(107)	1.96	(53)	15.72	(66)	16.97	(37)
	gnt (9)	43.24	(25)	0.23	(4)	21.53	(108)	0.18	(4)	10.52	(53)	18.27	(95)
GV10-83-9	gl (6)	51.42	(28)	1.95	(3)	19.20	(56)	0.01	(2)	7.70	(15)	7.78	(12)
$F = 0.07$	ol (11)	40.19	(34)	0.02	(2)	0.06	(3)	0.03	(3)	14.50	(14)	45.13	(22)
	cpx (11)	50.88	(26)	0.51	(3)	8.02	(23)	0.14	(4)	5.55	(19)	16.81	(26)
	opx (8)	52.49	(90)	0.22	(4)	7.80	(87)	0.14	(2)	9.02	(12)	28.73	(44)
	sp (6)	0.32	(18)	0.20	(6)	64.05	(164)	2.32	(43)	13.59	(180)	18.88	(59)
GV10-83-10	gl (10)	49.27	(34)	0.92	(21)	16.33	(46)	0.04	(2)	9.38	(21)	10.45	(47)
$F = 0.13$	ol (8)	40.69	(19)	0.02	(3)	0.11	(4)	0.04	(3)	12.92	(27)	46.39	(36)
	cpx (12)	50.34	(62)	0.42	(10)	8.49	(81)	0.17	(3)	5.13	(28)	17.24	(51)
	sp (5)	0.24	(11)	0.26	(4)	65.48	(39)	2.95	(13)	11.62	(30)	19.05	(13)
GV10-83-13	gl (15)	47.76	(36)	0.71	(8)	16.00	(18)	0.05	(3)	9.70	(24)	11.49	(42)
$F = 0.19$	ol (12)	40.22	(27)	0.02	(3)	0.11	(5)	0.04	(4)	11.99	(31)	46.92	(50)
	cpx (18)	50.19	(56)	0.36	(7)	8.64	(76)	0.23	(5)	4.44	(41)	17.78	(42)
	sp (4)	0.34	(19)	0.19	(6)	64.28	(139)	3.14	(57)	12.03	(100)	19.56	(60)
GV10-83-18	gl (10)	46.94	(20)	0.66	(5)	15.40	(19)	0.05	(3)	9.18	(13)	12.22	(14)
$F = 0.31$	ol (13)	40.60	(27)	0.02	(1)	0.10	(5)	0.05	(3)	10.92	(9)	48.07	(57)
	cpx (14)	50.48	(37)	0.34	(5)	8.80	(56)	0.24	(5)	4.10	(30)	17.62	(20)
	sp (4)	0.24	(8)	0.17	(2)	65.09	(107)	3.75	(24)	8.84	(24)	21.97	(21)
GV10-83-15	gl (9)	46.55	(88)	0.64	(2)	14.85	(55)	0.06	(2)	8.71	(48)	12.95	(7)
$F = 0.42$	ol (17)	40.47	(27)	0.04	(2)	0.07	(4)	0.04	(3)	10.73	(15)	48.39	(43)

Table 3 continued

Run	Phase	SiO$_2$		TiO$_2$		Al$_2$O$_3$		Cr$_2$O$_3$		FeO		MgO	
	cpx (17)	51.01	(66)	0.23	(3)	8.27	(69)	0.23	(7)	3.86	(11)	18.50	(33)
	sp (5)	0.28	(10)	0.15	(4)	66.50	(52)	3.91	(66)	8.89	(19)	22.06	(11)
GV10-83-21	gl (9)	46.87	(26)	0.63	(15)	13.97	(16)	0.05	(2)	8.49	(33)	13.54	(43)
$F = 0.52$	ol (17)	40.60	(26)	0.02	(2)	0.08	(3)	0.05	(2)	10.09	(76)	48.39	(53)
	cpx (17)	50.47	(51)	0.22	(6)	8.39	(50)	0.33	(9)	3.85	(19)	19.11	(19)
GV10-83-22	gl (9)	47.76	(32)	0.58	(7)	11.93	(38)	0.11	(3)	6.71	(4)	15.23	(38)
$F = 0.88$	ol (17)	41.70	(22)	0.01	(2)	0.10	(2)	0.07	(4)	7.40	(14)	49.53	(29)

Run	Phase	CaO		Na$_2$O		K$_2$O		Total		X_{Mg}		CIPW[a]
Exp. at 1 GPa												
GV10-83-4	ol (10)	0.41	(4)	0.01	(1)	–		99.91	(71)	0.83	(0)	
$F = 0$	cpx (15)	19.00	(56)	0.66	(6)	0.09	(0)	100.37	(51)	0.84	(1)	
	opx (9)	1.93	(68)	0.04	(3)	–		99.52	(79)	0.84	(0)	
	sp (10)	0.24	(5)	0.01	(2)	–		99.02	(32)	0.68	(1)	
GV10-83-1	gl (11)	10.47	(57)	2.17	(15)	0.44	(12)	98.67	(46)	0.53	(2)	4/20/8/0/64
$F = 0.02$	ol (18)	0.48	(13)	0.01	(1)	–		100.81	(48)	0.83	(0)	
	cpx (17)	17.89	(31)	0.34	(4)	0.01	(0)	100.19	(42)	0.84	(0)	
	opx (16)	2.11	(13)	0.05	(3)	–		100.37	(37)	0.85	(0)	
	sp (4)	0.22	(3)	0.01	(1)	–		99.84	(59)	0.68	(1)	
GV10-83-2	gl (12)	12.38	(57)	1.41	(11)	0.27	(7)	99.23	(70)	0.66	(1)	1/26/20/0/51
$F = 0.13$	ol (17)	0.44	(9)	0.01	(1)	–		100.57	(47)	0.86	(1)	
	cpx (18)	17.67	(77)	0.29	(4)	0.02	(1)	100.30	(36)	0.86	(1)	
	sp (10)	0.26	(7)	0.01	(1)	0.01	(0)	100.34	(86)	0.74	(2)	
GV10-83-14	gl (8)	13.84	(9)	0.84	(8)	0.15	(4)	99.25	(37)	0.73	(0)	0/16/27/12/44
F = 0.40	ol (8)	0.27	(8)	0.01	(1)	–		99.88	(26)	0.88	(0)	
	cpx (12)	19.24	(20)	0.22	(3)	0.02	(0)	100.24	(56)	0.88	(0)	
	sp (5)	0.27	(4)	0.00	(0)	–		99.52	(42)	0.77	(1)	
GV10-83-6	gl (13)	14.49	(68)	0.66	(7)	0.12	(8)	98.71	(75)	0.75	(1)	0/13/30/14/41
$F = 0.57$	ol (12)	0.45	(3)	0.01	(1)	–		100.04	(33)	0.90	(0)	
	cpx (16)	19.69	(38)	0.18	(2)	0.01	(0)	99.85	(40)	0.90	(1)	
GV10-83-8	gl (15)	15.77	(28)	0.46	(6)	0.08	(1)	98.79	(29)	0.79	(1)	0/9/40/17/34
$F = 0.91$	ol (11)	0.51	(2)	0.00	(0)	–		100.34	(26)	0.92	(0)	
Exp. at 1.5 GPa												
GV10-83-16	ol (6)	0.38	(3)	0.01	(1)	–		99.53	(35)	0.83	(0)	
$F = 0$	cpx (13)	17.74	(32)	0.75	(3)	0.11	(0)	100.89	(22)	0.84	(0)	
	opx (9)	1.82	(9)	0.05	(2)	–		99.80	(57)	0.85	(0)	
	sp (4)	0.28	(12)	0.01	(1)	–		98.56	(150)	0.66	(1)	
	gnt (9)	6.89	(87)	0.04	(3)	0.01	(0)	100.90	(64)	0.76	(1)	
GV10-83-9	gl (6)	8.21	(22)	1.99	(10)	0.38	(6)	98.71	(55)	0.64	(1)	4/31/0/0/61
$F = 0.07$	ol (11)	0.41	(5)	0.01	(1)	–		100.34	(22)	0.84	(1)	
	cpx (11)	18.00	(29)	0.42	(4)	0.03	(1)	100.36	(36)	0.84	(0)	
	opx (8)	2.12	(14)	0.05	(3)	–		100.57	(36)	X_{Mg}	(0)	
	sp (6)	0.26	(8)	0.01	(1)	0.01	(0)	99.62	(35)	0.71	(3)	
GV10-83-10	gl (10)	10.41	(52)	1.55	(24)	0.26	(8)	98.61	(55)	0.66	(1)	0/27/12/7/52
$F = 0.13$	ol (8)	0.47	(14)	0.01	(1)	–		100.65	(28)	0.86	(0)	
	cpx(12)	17.75	(83)	0.37	(7)	0.04	(1)	99.95	(46)	0.86	(1)	
	sp (5)	0.28	(10)	0.00	(0)	0.01	(0)	99.90	(49)	0.75	(1)	
GV10-83-13	gl (15)	11.82	(29)	1.26	(22)	0.21	(2)	99.10	(35)	0.68	(2)	0/16/17/16/50
$F = 0.19$	ol (12)	0.40	(13)	0.01	(1)	–		99.70	(44)	0.87	(0)	

Table 3 continued

Run	Phase	CaO		Na$_2$O		K$_2$O		Total		X_{Mg}		CIPW[a]
	cpx (18)	17.67	(69)	0.26	(2)	0.03	(1)	99.61	(50)	0.88	(1)	
	sp (4)	0.35	(6)	0.01	(1)	–		99.89	(39)	0.74	(2)	
GV10-83-18	gl (10)	13.16	(22)	0.94	(2)	0.18	(9)	98.73	(17)	0.70	(1)	0/11/23/18/47
$F = 0.31$	ol (13)	0.36	(6)	0.01	(1)	–		100.12	(30)	0.88	(0)	
	cpx (14)	18.05	(55)	0.21	(3)	0.02	(0)	99.88	(49)	0.88	(1)	
	sp (4)	0.16	(4)	0.00	(0)	–		100.21	(112)	0.82	(1)	
GV10-83-15	gl (9)	14.16	(67)	0.69	(8)	0.12	(8)	98.72	(26)	0.72	(1)	0/8/27/19/44
$F = 0.42$	ol (17)	0.26	(6)	0.01	(1)	–		99.99	(36)	0.88	(0)	
	cpx (17)	18.24	(44)	0.19	(4)	0.05	(1)	100.58	(46)	0.90	(0)	
	sp (5)	0.15	(5)	0.00	(1)	0.01	(0)	101.96	(58)	0.82	(0)	
GV10-83-21	gl (9)	14.76	(43)	0.58	(9)	0.11	(6)	99.02	(39)	0.74	(1)	0/8/31/19/41
$F = 0.52$	ol (17)	0.46	(7)	0.01	(1)	–		99.69	(49)	0.89	(1)	
	cpx (17)	17.12	(28)	0.17	(3)	0.04	(3)	99.69	(39)	0.90	(1)	
GV10-83-22	gl (9)	15.65	(21)	0.46	(5)	0.12	(11)	98.55	(49)	0.80	(0)	0/8/38/17/35
$F = 0.88$	ol (17)	0.49	(3)	0.03	(2)	–		99.33	(35)	0.92	(0)	

Numbers in parentheses correspond to 1σ standard deviations, given in terms of the least unit cited; e.g., 5.2 (29) and 74.4 (27) represent 5.2 ± 2.9 and 74.4 ± 2.7, respectively

gl glass, *ol* olivine, *cpx* clinopyroxene, *opx* orthopyroxene, *sp* spinel, *gnt* garnet. Along with the phase, we report the number of analyses in parentheses

[a] CIPW norms: quartz/hypersthene/diopside/olivine/feldspars. "*F*" below the run label is the melt fraction calculated in each experiments

Solidus temperature and melt productivity

The solidus of pyroxenite GV10 is between 1180 and 1200 °C at 1 GPa, and between 1230 and 1250 °C at 1.5 GPa (Fig. 6). At pressure of 1 and 1.5 GPa, pyroxenite GV10 starts melting at lower temperature, compared to all fertile lherzolites experimentally investigated (Fig. 6).

Melt fraction vs. temperature trends at both 1 and 1.5 GPa are concave upward, suggesting that isobaric melt productivity (d*F*/d*T*)$_P$ increases with temperature (Fig. 7), in agreement with previous experimental results on pyroxenite or eclogite compositions (e.g., Pickering-Witter and Johnson 2000; Kogiso and Hirschmann 2001; Pertermann and Hirschmann 2003b; Lambart et al. 2009a), and thermodynamic models of peridotite partial melting (i.e. Hirschmann et al. 1999; Asimow et al. 2001). At both pressures, the isobaric melt productivity at low melting degrees (*F* < 12.6%) is about 0.2%/°C (Fig. 7). At higher melting degrees (*F* > 12.6%), the mean isobaric productivity is 0.9%/°C at 1 GPa and 0.6%/°C at 1.5 GPa (Fig. 7).

Discussion

Melting and phase relations

Phase abundances and glass proportions have been calculated by weighted least squares mass balance that included nine oxides, SiO$_2$, TiO$_2$, Al$_2$O$_3$, Cr$_2$O$_3$, FeO, MgO, CaO, Na$_2$O and K$_2$O. Detailed explanation of mass balance calculations is reported in Borghini et al. (2010).

In the pressure and temperature range investigated in this study, olivine is stable along the whole melting range with low modal abundances (<14%; Table 2; Fig. 8). Clinopyroxene is the dominant phase in GV10 pyroxenite residual assemblage (Table 2; Fig. 8). Spinel persists over than 40% of melt fraction at both pressures (Table 2; Fig. 8). Orthopyroxene disappears from the residue at F higher than 12%, and low modal abundance of garnet is stable only in the subsolidus assemblage at 1.5 GPa (Table 2; Fig. 8). The sequence of mineral phases disappearance at increasing melt fraction is, therefore, orthopyroxene–spinel–clinopyroxene–olivine and garnet–orthopyroxene–spinel–clinopyroxene–olivine, at 1 and 1.5 GPa, respectively.

To constrain the stoichiometry of reactions controlling the consumption of mineral phases along the melting interval of GV10, we performed mass balance calculations (within the same chemical system used for determination of modal abundances, see above), using the mineral and glass compositions at the beginning and the end of each phase exhaustion step with increasing melt fraction. Average melting reactions for pyroxenite GV10 are reported in Table 4, together with those for pyroxenites and peridotites at 1 and 1.5 GPa available in the literature. Melting reactions in pyroxenite GV10 at 1.5 GPa
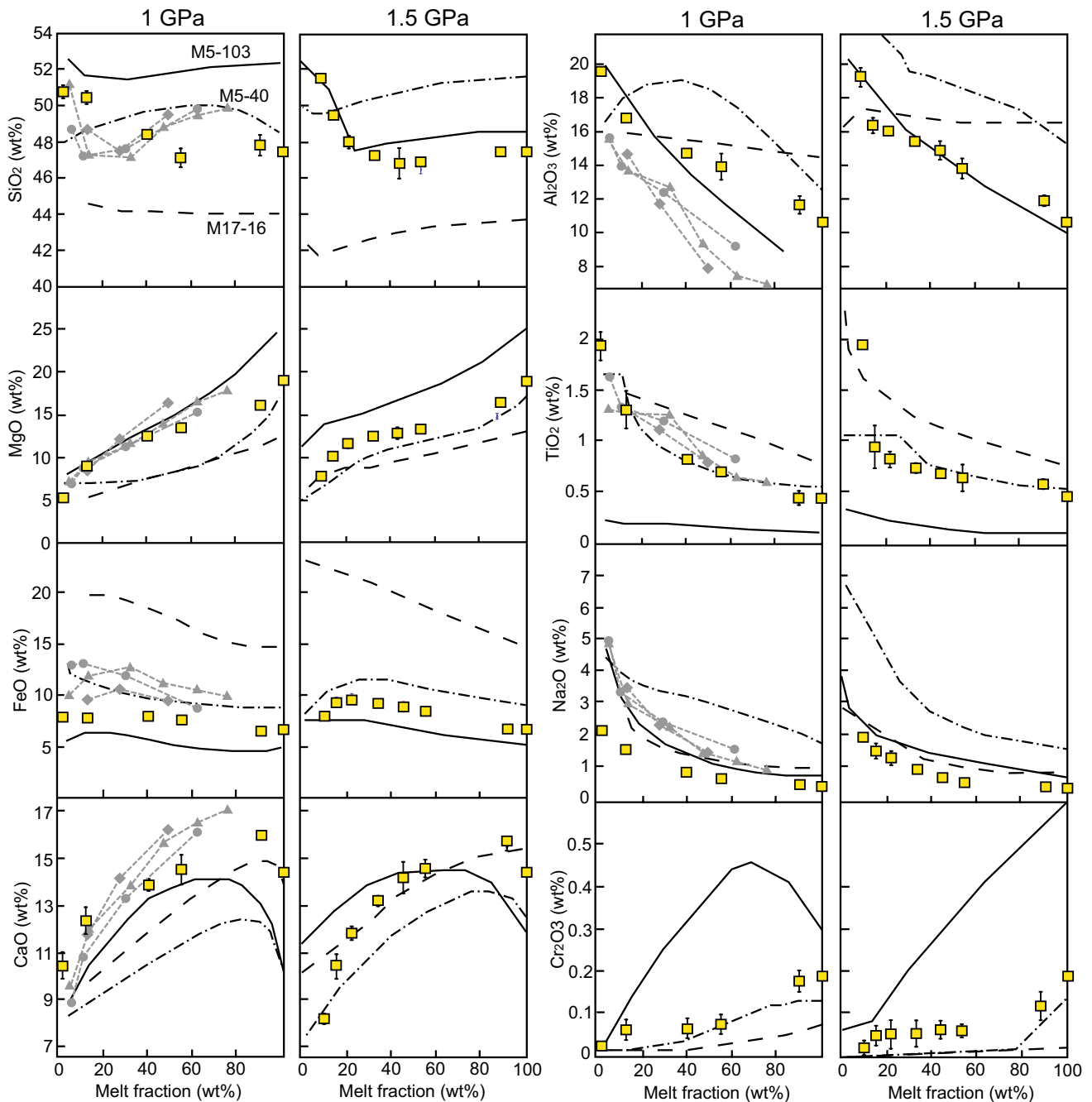
Fig. 3 Oxide concentrations in experimental melts plotted as a function of melt fractions (wt%). Data plotted at $F = 100\%$ correspond to the bulk-rock composition. Also reported for comparison are trends (*black lines*) extrapolated by melting experiments at 1 and 1.5 GPa on three silica-deficient pyroxenites by Lambart et al. (2009a). *Grey symbols* linked by *dotted lines* are experimental results at 1 GPa on clinopyroxenite bulks (Kogiso and Hirschmann 2001). Comparison between the compositions of melts produced by GV10 at 1 and 1.5 GPa is illustrated in Supplementary Figure 2

are similar to those at 1 GPa, except for the first melting interval at 1.5 GPa in which garnet is rapidly consumed (reaction 14, Table 4).

Although the melting relation opx + cpx + sp → liq + ol is the same for pyroxenites and peridotite (Table 4), the contribution of orthopyroxene with respect to clinopyroxene is higher when pyroxenite is considered, as suggested for example by reaction 1 at 1 GPa (Table 4):

0.86 opx + 0.57 cpx + 0.08 sp = 1 liq + 0.51 ol
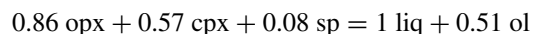
This results in rapid consumption of orthopyroxene during melting, and is likely related to the high CaO content in
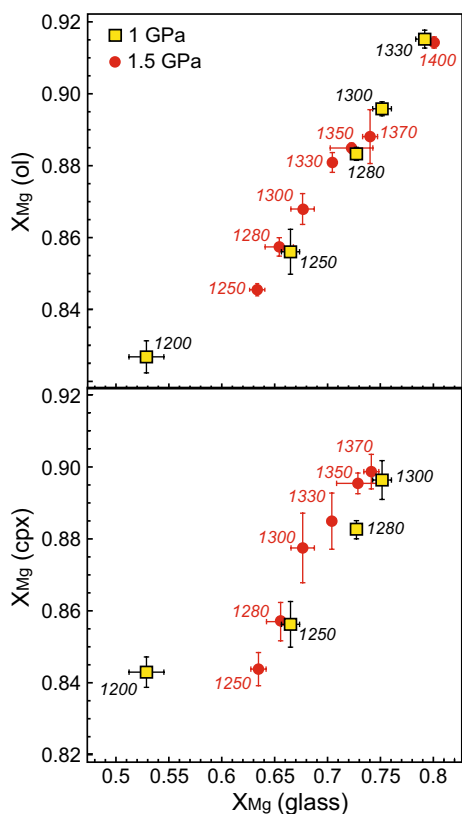
Fig. 4 Fe-Mg partitioning of glass vs. olivine and clinopyroxene. $X_{Mg} = Mg/(Mg + Fe^{tot})$
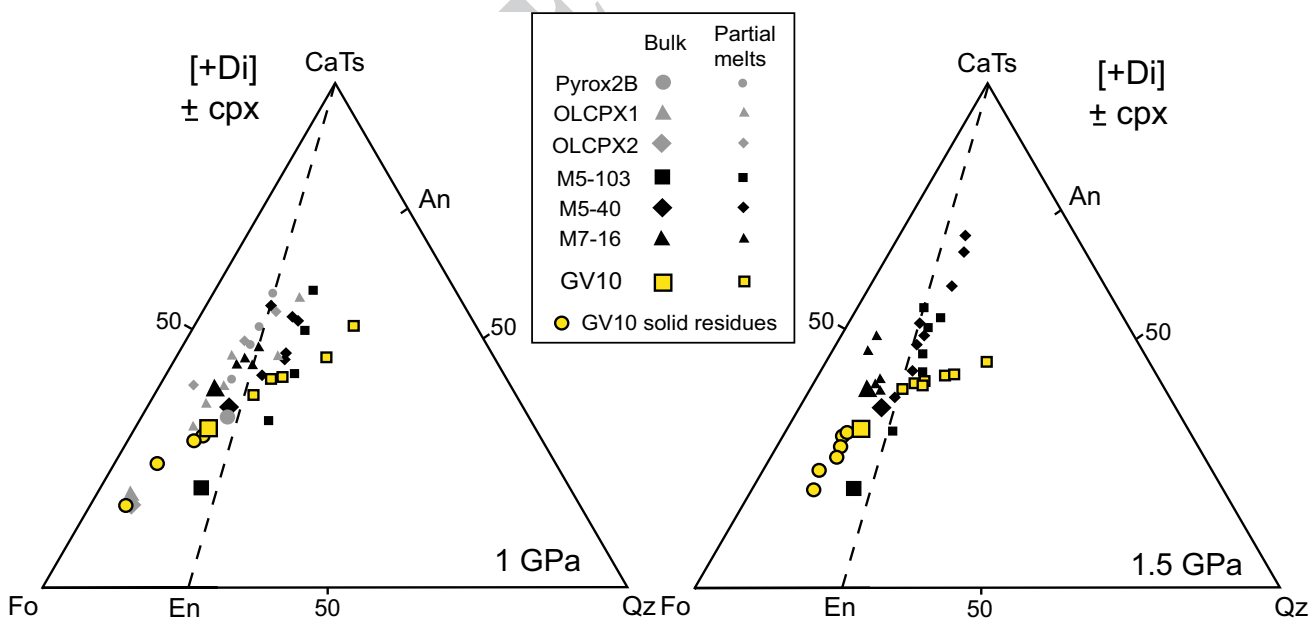
the bulk rock (Fig. 1), favoring the stabilization of clinopy-roxene over orthopyroxene in the residue. Similar melting relation was documented in other pyroxenites and clinopy-roxene-rich lherzolites (e.g., FER-B, Pickering-Witter and Johnson 2000; M5-103, Lambart et al. 2009a).

At F higher than 12%, clinopyroxene is the main phase that contributes to melting, with minor contribution of spi-nel until its exhaustion (Table 4; Fig. 8), following the aver-age reaction (e.g., at 1 GPa, reaction 2, Table 4):

$$0.97 \text{ cpx} + 0.1 \text{ sp} = 1 \text{ liq} + 0.07 \text{ ol}$$
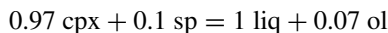
The coefficients are comparable to those obtained in previ-ous experimental works on anhydrous pyroxenites and clino-pyroxene-rich peridotites (reactions 5 and 6, Table 4). Around $F = 90\%$, clinopyroxene is also consumed and olivine is the liquidus phase (reactions 3 and 17, Table 4; Fig. 8).

As expected, along the whole melting interval, residual phases show progressively higher X_{Mg} values at increasing melt fraction (Table 3; Fig. 4). At low melting degrees, the high coefficient of orthopyroxene involved in the melting reaction (reactions 1, 14 and 15, Table 4) results in rela-tively high SiO_2 content in partial melts at both pressures (Fig. 3). After orthopyroxene exhaustion, melt composition is controlled by the composition of coexisting clinopyrox-ene and, to a lesser extent, spinel. CaO content of partial melts increases with melt fraction until the disappearance of clinopyroxene (Fig. 3).

Fig. 5 Molar projections from diopside [Di] onto the pseudo-ternary diagram forsterite (Fo)—calcium tschermak (CaTs)—quartz (Qz) (O'Hara 1972) of melts produced by experiments on GV10 at 1 and 1.5 GPa. The *small yellow circles* represent the composition of solid residues calculated using the modes and composition of residual

minerals in experimental charges. The melt compositions reported in previous experimental studies on other pyroxenites are also reported (Lambart et al. 2009a; Kogiso and Hirschmann 2001). *Symbols* are as in Fig. 1. *Larger symbols* represent the starting materials
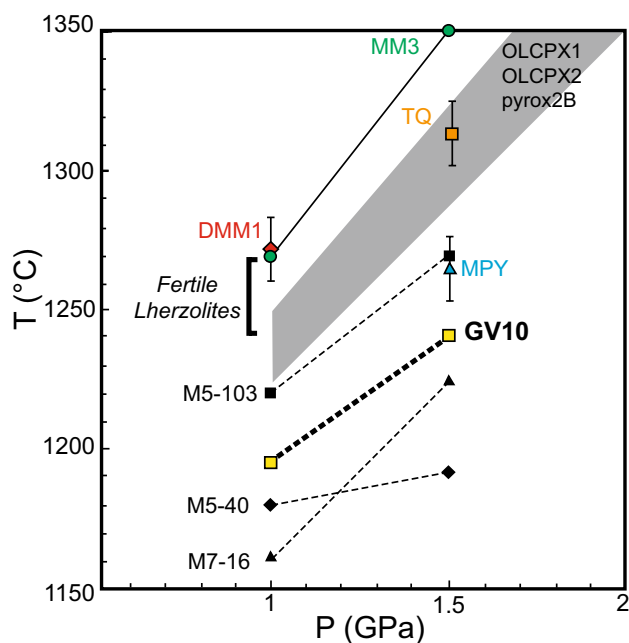
Fig. 6 Experimentally determined solidus temperature at 1 and 1.5 for pyroxenite GV10 compared to other pyroxenites and peridotites. Pyroxenites are: M5-103, M5-40 and M7-16 studied by Lambart et al. (2009a); OLCPX1, OLCPX2 and pyrox2B by Kogiso and Hirschmann (2001). Peridotites are: lherzolite MM3 (Falloon et al. 2008), fertile lherzolite MPY and depleted lherzolite TQ (Robinson et al. 1998), depleted lherzolite DMM1 (Wasylenki et al. 2003). Symbols are as in Fig. 1. Temperature interval named "Fertile peridotite" at 1.0 GPa includes experiments of variably fertile lherzolites from Pickering-Witter and Johnson (2000) and Schwab and Johnston (2001)

Fig. 7 Temperature-melt fraction curves determined at 1 GPa (**a**) and 1.5 GPa (**b**) for pyroxenite GV10 (*yellow squares*) compared to those extrapolated by previous experimental work on dry pyroxenite and peridotite: (1) pyroxenites M5-103, M5-40 and M7-16 from Lambart et al. (2009a); (2) clinopyroxenites Pyrox2B, OLCPX1 and OLCPX2 from Kogiso and Hirschmann (2001); (3) lherzolite MM3 from Baker et al. (1995) (*green squares*) and Falloon et al. (2008) (*green circles*)

553 The most striking compositional feature observed in
554 clinopyroxene is the decrease in jadeite component with
555 increasing melt fraction. As a whole, the low Na$_2$O contents
556 in melts (see Fig. 3) reflect relatively high partition coefficient
557 cient of Na between residual clinopyroxene and partial melt
558 ($D_{Na_2O}^{cpx/liquid}$). As shown in Fig. 9, $D_{Na_2O}^{cpx/liquid}$ calculated from
559 experiments on pyroxenite GV10 are positively correlated
560 with pressure and temperature. The increase of $D_{Na_2O}^{cpx/liquid}$
561 with pressure observed in GV10 experiments is well correlated
562 related with the $D_{Na_2O}^{cpx/liquid}$ calculated from experiments at 2
563 and 2.5 GPa on pyroxenites with comparable bulk composition
564 sition (MIX1G, Hirschmann et al. 2003; M5-40, Lambart
565 et al. 2013) (Fig. 9a). This overall correlation is in good
566 agreement with available quantitative models for Na partitioning
567 titioning between clinopyroxene and silicate melt (Blundy
568 et al. 1995; Villiger et al. 2007), as well as with the trend
569 defined by fitting literature experimental data (Villiger et al.
570 2007) (Fig. 9a).
571 On the other hand, the correlation of Na cpx/liquid partitioning
572 titioning with temperature has been poorly discussed in the
573 literature. Figure 9b reports a compilation of $D_{Na_2O}^{cpx/liquid}$,
574 derived from experiments on fertile peridotites and

575 pyroxenites at 0.7–2.5 GPa (see the figure caption for references).
576 erences). Overall, these data point to a positive correlation
577 of Na cpx/liquid partitioning with temperature (Fig. 9b).
578 Blundy et al. (1995) argued that, at 1 GPa, temperature
579 dependence of $D_{Na_2O}^{cpx/liquid}$ is greatly subordinate to that of
580 pressure. In fractional crystallization experiments, Villiger
581 et al. (2007) observed that the Na distribution coefficients
582 between clinopyroxene and liquid decrease at decreasing
583 temperature, as observed in our experiments (Fig. 9b), but
584 they concluded that a clear relationship between Na partitioning
585 tioning and temperature cannot be established. Our results
586 corroborate the existence of such correlation, although a
587 proper understanding of factors controlling such relationship
588 ship would need a more focused study.
589 Similar to Na$_2$O, Al$_2$O$_3$ and TiO$_2$ behave as incompatible
590 elements (Fig. 3), whereas Cr$_2$O$_3$ is compatible and mostly
591 partitioned in residual spinel (Table 3; Fig. 3).

Comparison with previous studies

593 The solidus of GV10 at 1 and 1.5 GPa is located at lower temperature
594 perature with respect to experimental results on variably fertile
595 tile lherzolites (Pickering-Witter and Johnson 2000; Schwab
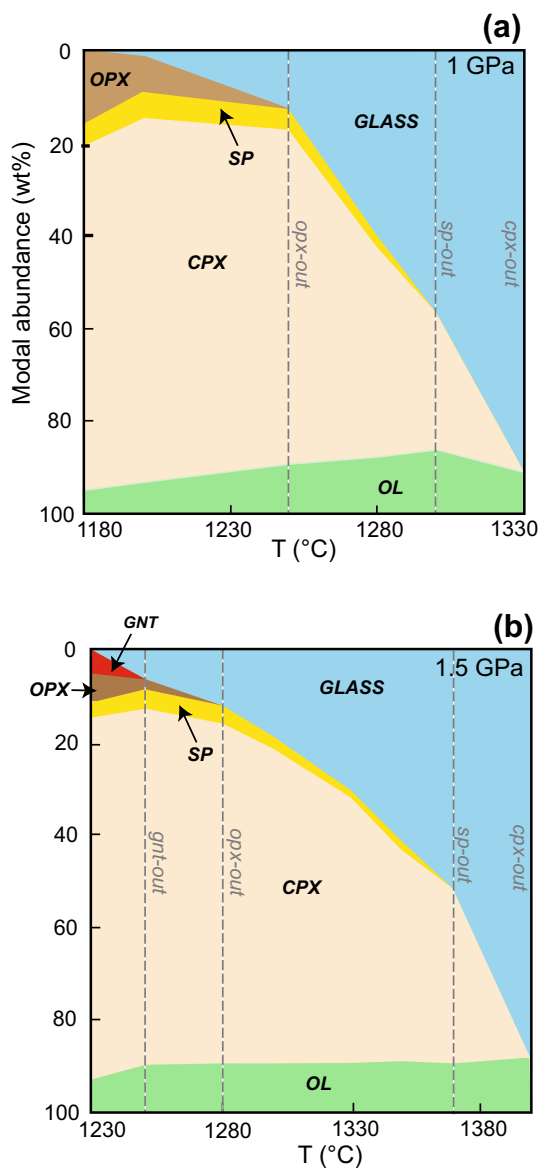596 and Johnston 2001) and clinopyroxenites investigated by

Fig. 8 Modal abundance calculated by weighted least squares mass balance in experiments at 1 GPa (**a**) and 1.5 GPa (**b**) as a function of temperature. The *grey dotted lines* represent the temperature of mineral phases disappearance. *ol* olivine, *cpx* clinopyroxene, *opx* orthopyroxene, *sp* spinel, *gnt* garnet

Kogiso and Hirschmann (2001) (Fig. 6). Melting experiments at 1 GPa on these clinopyroxenites have clinopyroxene + olivine as residual minerals (Kogiso and Hirschmann 2001). In our experiments, the stability of residual spinel, in addition to clinopyroxene and olivine, likely resulted from higher Al_2O_3 content of pyroxenite GV10 (Table 1). Lower CaO and higher MgO contents in GV10 could have enhanced minor modal orthopyroxene (Tables 1, 2), never found in clinopyroxenites (Kogiso and Hirschmann 2001).

The solidus curve and the isobaric melt productivity $(dF/dT)_P$ of pyroxenite GV10 are in agreement with the data reported for pyroxenites previously investigated by Lambart et al. (2009a) (Fig. 7). In particular, pyroxenite GV10 displays solidus and melt productivity curves intermediate between M5-40 and M5-103 (Figs. 6, 7).

According to Kogiso et al. (2004a), alkali contents and X_{Mg} of the bulk composition mostly influence the solidus temperatures of natural anhydrous pyroxenites. On this basis, Lambart et al. (2016) have recently proposed an empirical parameterization to derive the melt fraction versus temperature from 5% melting up to clinopyroxene disappearance for pyroxenites as a function of pressure, temperature and bulk composition. Pyroxenite GV10 has X_{Mg} and $(Na_2O + K_2O)$ lower than M5-103 (Table 1). The model successfully predicts the relative location of the $(dF/dT)_P$ between GV10 and pyroxenites studied by Lambart et al. (2009a), but locates this curve at slightly higher temperature with respect to the curve extrapolated by the experiments.

The most important differences in the melting relations between GV10 and the pyroxenites M5-40 and M5-103 of Lambart et al. (2009a) are the presence of plagioclase and the abundance of spinel. Both M5-40 and M5-103 have plagioclase in the subsolidus assemblage at 1 GPa, 30 and 4%, respectively, whereas plagioclase is not stable in GV10 pyroxenite. This is due to the much lower Na_2O/CaO ratio of GV10, which tends to stabilize plagioclase at lower pressure (Green and Falloon 1998; Borghini et al. 2010). Spinel is present in very low modal abundance (<1%) or absent in the experiments on M5-40 and M5-103. At 1.5 GPa, spinel is absent in M5-103 but it is present at near-solidus conditions in equilibrium with plagioclase and garnet in the M5-40 (Lambart et al. 2009a).

The variational trends of MgO and FeO abundances in melts at both 1 and 1.5 GPa obtained for pyroxenite GV10 are similar to those of M5-40 and M5-103, with absolute contents mostly varying at intermediate values (Fig. 3), according to the bulk compositions (Table 1). TiO_2 and Cr_2O_3 compositional trends defined by GV10 melts follow those observed for M5-40 pyroxenite, except for the higher TiO_2 contents in GV10 at low F. Progressive Al_2O_3 content decrease with increasing F at both pressures is similar to what observed for M5-103, but with a lower slope, because spinel is a residual phase up to relatively higher F in GV10 pyroxenite. The high CaO contents of GV10 melts mimic those documented in melts produced by clinopyroxenites at 1 GPa (Kogiso and Hirschmann 2001), and by garnet-olivine clinopyroxenite M7-16 at 1.5 GPa (Lambart et al. 2009a) (Fig. 3). At both investigated pressure conditions, the variation of SiO_2 contents in GV10 melts defines a trajectory of rapid decrease at low F and a slight increase at higher F, similar to M5-103 but more accentuated (Fig. 3). This trend results by early exhaustion of orthopyroxene and

Table 4 Melting reactions (wt%) for pyroxenites and peridotites at 1 and 1.5 Gpa

Reference	Lithotype	Bulk	Melting interval	Melting reactions	R-n[a]
1 GPa					
This study	pyrox	GV10	Solidus to opx-out	0.86 opx + 0.57 cpx + 0.08 sp = 1 liq + 0.51 ol	1
			opx-out to sp-out	0.97 cpx + 0.1 sp = 1 liq + 0.07 ol	2
			sp-out to cpx-out	1.04 cpx = 1 liq + 0.04 ol	3
Lambart et al. (2009)	pyrox	M5-103	Main reaction	0.49 opx + 0.61 cpx = 1 liq + 0.10 ol	4
	pyrox	M7-16	Main reaction	0.95 cpx + 0.1 sp = 1 liq + 0.05 ol	5
Pickering-Witter and Johnson (2000)	perid	FER-B	Solidus to cpx-out	0.99 cpx + 0.05 sp = 1 liq + 0.04 ol	6
	perid	FER-D	Solidus to cpx-out	0.14 opx + 0.75 cpx + 0.17 sp = 1 liq + 0.06 ol	7
	perid	FER-E	Solidus to cpx-out	0.27 opx + 0.78 cpx + 0.05 sp = 1 liq + 0.10 ol	8
Baker and Stolper (1994)	perid	MM3	Main reaction	0.38 opx + 0.71 cpx + 0.13 sp = 1 liq + 0.22 ol	9
Falloon et al. (2008)	perid	MM3	Solidus to plag-out	0.14 ol + 0.31 opx + 0.81 plag = 0.75 liq + 0.48 cpx + 0.004 sp	10
			Plag-out to cpx-out	0.275 opx + 0.887 cpx + 0.052 sp = 1.036 liq + 0.178 ol	11
Wasylenki et al. (2003)	perid	DMM1	Solidus to cpx-out	0.56 opx + 0.72 cpx + 0.04 sp = 1 liq + 0.34 ol	12
			Above cpx + sp-out	1.24 opx = 1 liq + 0.24 ol	13
1.5 GPa					
This study	pyrox	GV10	Solidus to gnt-out	0.59 gnt + 0.82 opx + 0.18 cpx = 1 liq + 0.59 ol	14
			gnt-out to opx-out	0.87 opx + 0.49 cpx + 0.1 sp = 1 liq + 0.46 ol	15
			opx-out to sp-out	0.97 cpx + 0.09 sp = 1 liq + 0.06	16
			sp-out to cpx-out	1.07 cpx = 1 liq + 0.07	17
Falloon et al. (2008)	perid	MM3	Solidus to cpx-out	0.275 opx + 0.887 cpx + 0.052 sp = 1.036 liq + 0.178 ol	18
Robinson et al. (1998)	perid	MPY	0–1%	0.61 opx + 0.58 cpx + 0.001 sp = 1 liq + 0.19 ol	19
	perid	TQ	Main reaction	0.33 opx + 0.83 cpx + 0.08 sp = 1 liq + 0.24 ol	20

pyrox pyroxenite, *perid* peridotite, *opx* orthpyroxene, *cpx* clinopyroxene, *ol* olivine, *sp* spinel, *gnt* garnet, *plag* plagioclase, *liq* liquidus

[a] Reaction number (as discussed in the text)

late disappearance of spinel. Variation trends of Na_2O contents, marked by progressive decrease at increasing F, are similar to those documented for all pyroxenites at 1–1.5 GPa, but partial melts of GV10 display the lowest Na_2O absolute concentrations (Fig. 3), consistent with higher $D_{Na_2O}^{cpx/liquid}$ (Fig. 9). Differently from pyroxenites investigated by Lambart et al. (2009), no partial melts with nepheline-normative compositions are produced by GV10 pyroxenite at 1–1.5 GPa. By contrasts, at low melting degrees GV10 melts have quartz-normative compositions (Table 3).

Major element chemical signature of pyroxenite-derived melts

Lambart et al. (2013) highlighted that the determination of pyroxenite contribution in major element composition of oceanic basalts may be difficult because, at identical pressure and temperature conditions, many pyroxenitic melts are quite similar to peridotitic melts. Although many pyroxenites are expected to have lower X_{Mg} and higher TiO_2 and alkali contents, these chemical features are diluted in their partial melts by the higher degrees of melting compared to peridotites (e.g., Médard et al. 2006; Lambart et al. 2009a). However, some pyroxenites can produce SiO_2-poor and/or Fe-rich melts that are able to significantly affect the composition of melts produced by a pyroxenite–peridotite mixed mantle source. Accordingly, Lambart et al. (2013) identified a group of primitive MORB that represents the best candidates to preserve this pyroxenite signature, even after the mixing with peridotitic melts (px-MORB; with MgO ≥9 wt%, SiO_2 <48.8 wt% and FeO >8.3). Further major element markers for pyroxenite contribution, namely high CaO/Al_2O_3 ratios and high TiO_2 contents, have been proposed for OIBs (e.g., Prytulak and Elliot 2007; Jackson and Dasgupta 2008; Shorttle and Maclennan 2011). Moreover, primary magma calculations (PRIMELTS2.XLS, Herzberg and Asimow 2008) suggest that low CaO–MgO trends in some OIBs are not consistent with the composition of
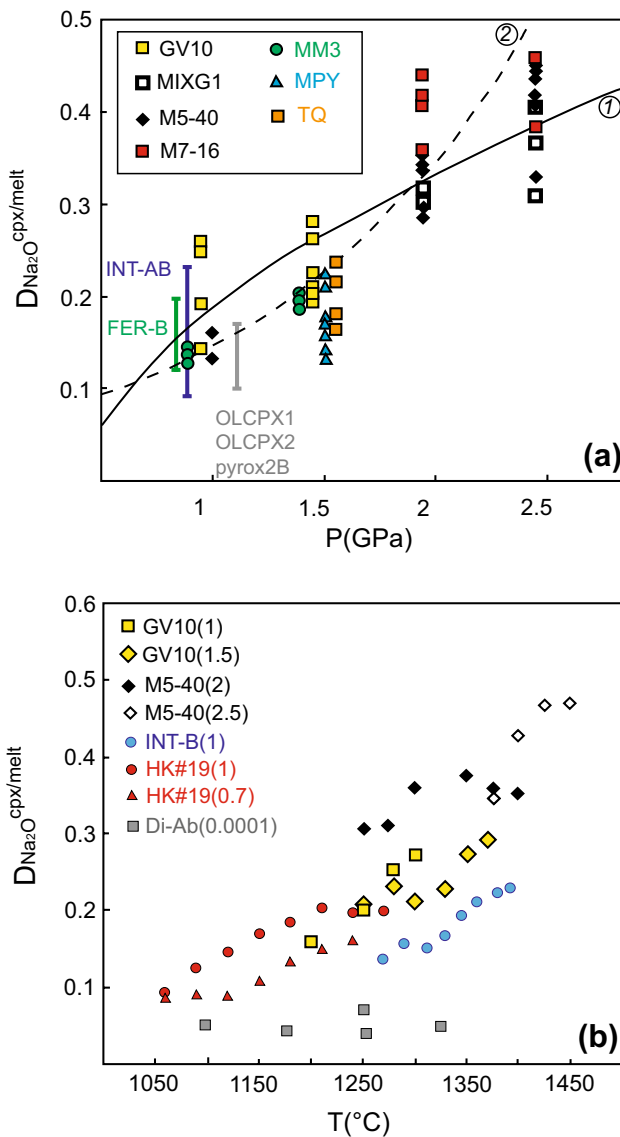
Fig. 9 Partitioning of Na_2O between clinopyroxene and glass ($D_{Na_2O}^{cpx/liquid}$) as a function of pressure (**a**) and temperature (**b**). Our data are compared with $D_{Na_2O}^{cpx/liquid}$ from experiments on lherzolites MM3 (Falloon et al. 2008), MPY and TQ (Robinson et al. 1998), fertile lherzolites FER-B (Pickering-Witter and Johnson 2000), INT-A and INT-B (Schwab and Johnston 2001), pyroxenites MIXG1 from Hirschmann et al. (2003), M5-40 and M7-16 from Lambart et al. (2009a), OLCPX1, OLCPX2 and pyrox2B from Kogiso and Hirschmann (2001). Data in the system diopside-albite are from Blundy et al. (1995) and from fractional and equilibrium crystallization experiments are by Villiger et al. (2007). Curves 1 and 2 in (**a**) refer to quantitative model proposed by Blundy et al. (1995) and fit of literature experimental data by Villiger et al. (2007), respectively. *Number between parenthesis* in (**b**) refer to experimental pressure (GPa)

699 melts from a pure peridotite and they can discriminate the
700 contribution of melts derived from a low-Ca pyroxene,
701 as the modeled olivine-free Px-1 (Sobolev et al. 2005,
702 2007).

703 To identify the major element signature of secondary
704 pyroxenite GV10, we compare the major element com-
705 position of melts produced in our experiments with those
706 of melts from experiments on various peridotite bulks,
707 at 1.0 and 1.5 GPa (Figs. 10, 11, see figure captions for
708 references). We only considered the melt compositions
709 produced at the same temperature interval investigated
710 in this study, i.e. 1200–1330 °C at 1 GPa and 1250–
711 1400 °C at 1.5 GPa.

712 GV10 melts span within almost the same MgO range
713 defined by experimental peridotitic melts (Figs. 10, 11),
714 except for low MgO contents at very low melting degree
715 ($F < 2\%$) and high MgO abundances in melts resulting
716 from F of about 90% at 1 GPa (Fig. 10).

717 At 1 GPa, SiO_2, TiO_2, FeO and Al_2O_3 abundances of
718 GV10 melts largely match the composition of many peri-
719 dotite-derived melts. However, at low melting degrees
720 GV10 melts display higher FeO and lower Al_2O_3 con-
721 tents relative to melts from a normal fertile lherzolite
722 (e.g., MM3, Fig. 10). Peculiar chemical features are the
723 CaO and Na_2O vs MgO trends (Fig. 10). At similar MgO,
724 pyroxenite GV10 tends to produce melts with higher CaO
725 and lower Na_2O contents than peridotite-derived melts
726 (Fig. 10). For high degrees of melting (i.e. the highest
727 MgO abundances), GV10 melts display CaO contents
728 much higher than all fertile lherzolites, but coupled to
729 very low Na_2O contents. Comparably low Na_2O abun-
730 dances are only observed in melts produced by moder-
731 ate melting degrees of depleted lherzolites (e.g., DMM1,
732 Wasylenki et al. 2003; Fig. 10).

733 At 1.5 GPa, GV10 melts resemble those of melts pro-
734 duced by very fertile lherzolites (e.g., lherzolite HK-66,
735 Hirose and Kushiro 1993, or refertilized lherzolites KG1
736 and KG2 from Kogiso et al. 1998), except for much lower
737 Na_2O contents in the entire pyroxenite melting interval,
738 and slightly lower SiO_2 coupled to higher CaO in high-
739 MgO pyroxenitic melts (Fig. 11). These latter also show
740 higher FeO and slightly lower Al_2O_3 and TiO_2 contents
741 compared to melts from a normal fertile lherzolite (e.g.,
742 MM3; Fig. 11).

743 In summary, as previously observed by Lambart et al.
744 (2009a, 2013), for many oxides the compositions of par-
745 tial melts from secondary pyroxenite GV10 are similar
746 or very close to those of melts produced by depleted and
747 variably fertile peridotites. The most striking geochemi-
748 cal signature of pyroxenite GV10 melts is their very low
749 Na_2O contents. In addition, they display higher CaO and
750 slightly lower Al_2O_3 concentrations, thus resulting in
751 higher CaO/Al_2O_3 ratio than peridotitic melts. In the next
752 section, we discuss to what extent the GV10 chemical
753 signature can impact the compositions of melts produced
754 by decompressional melting of a mixed pyroxenite–peri-
755 dotite mantle source at MOR settings.

Fig. 10 Compositions (in wt%) of GV10 partial melts at 1.0 GPa from this study compared with those of experimental melts from variably fertile and depleted lherzolites within the temperature range 1200–1330 °C


Legend:
- ☐ GV10 (this study)
- ☐ MM3 (Falloon et al. 1999, 2008)
- ◆ DMM1 (Wasylenki et al. 2003)
- ■ KLB-1
- ▲ HK-66 } Hirose and Kushiro (1993)
- ☐ FER-B
- ● FER-D } Pickering-Witter and Johnson (2000)
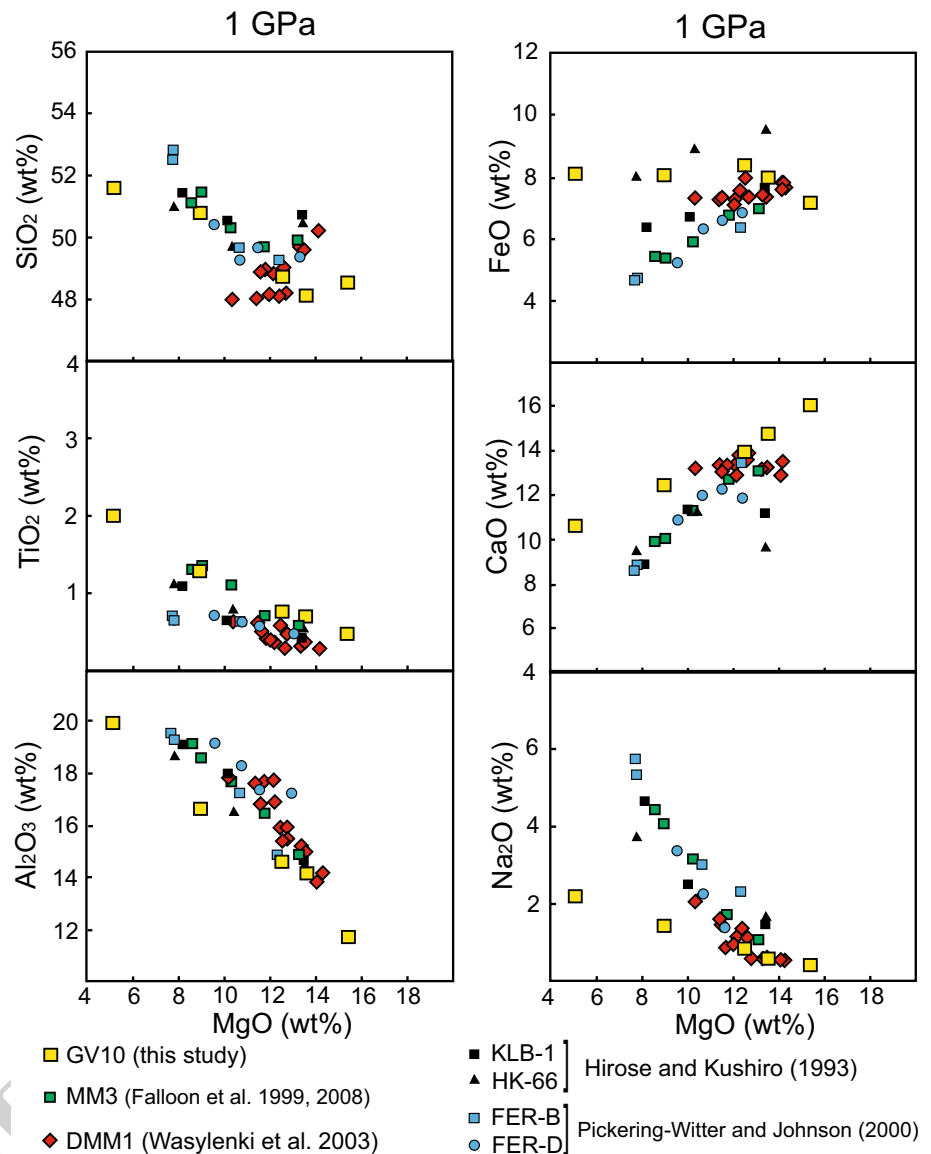
Secondary pyroxenites in heterogeneous upwelling mantle

Experimental results on secondary pyroxenite GV10 can be used to derive information on the composition of melts produced by adiabatic upwelling and melting of heterogeneous mantle sources. In our modeling, we envisage that mantle portions made by different proportions of pyroxenite GV10 and fertile lherzolite rise along mantle adiabats assuming a range of mantle potential temperatures (T_P) consistent with mantle melting at MOR settings ($T_P = 1260$–1430 °C; e.g., Langmuir et al. 1992; Shen and Forsyth 1995; Green et al. 2001; Presnall et al. 2002; Herzberg et al. 2003). At this purpose, we applied the recent parameterization of Lambart et al. (2016) that provides a method to simulate the decompression melting of mixed pyroxenite–peridotite mantle sources. Specifically, this model predicts the melt productivity of the two melting components at a given T_P of the rising mantle, as a function of bulk composition and mass fraction of pyroxenite (Lambart et al. 2016), using a modified version of the thermodynamic treatment of adiabatic fractional melting by Phipps Morgan (2001).

In the calculations, we assumed the parameterization of the peridotite solidus temperature proposed by Hirschmann (2000), which predicts slightly higher solidus temperature than Katz's parameterization adopted by Lambart et al. (2016), and is more consistent with experimental results on fertile lherzolite (e.g., Falloon et al. 2008) (see Fig. 6). Using Lambart et al. (2016) modeling, pyroxenite GV10 starts to melt at higher pressure than peridotites, consistent with experimental results (Fig. 6).

Fig. 11 Compositions (in wt%) of GV10 partial melts at 1.5 GPa from this study compared with those of experimental melts from variably fertile and depleted lherzolites within the temperature range 1250–1400 °C
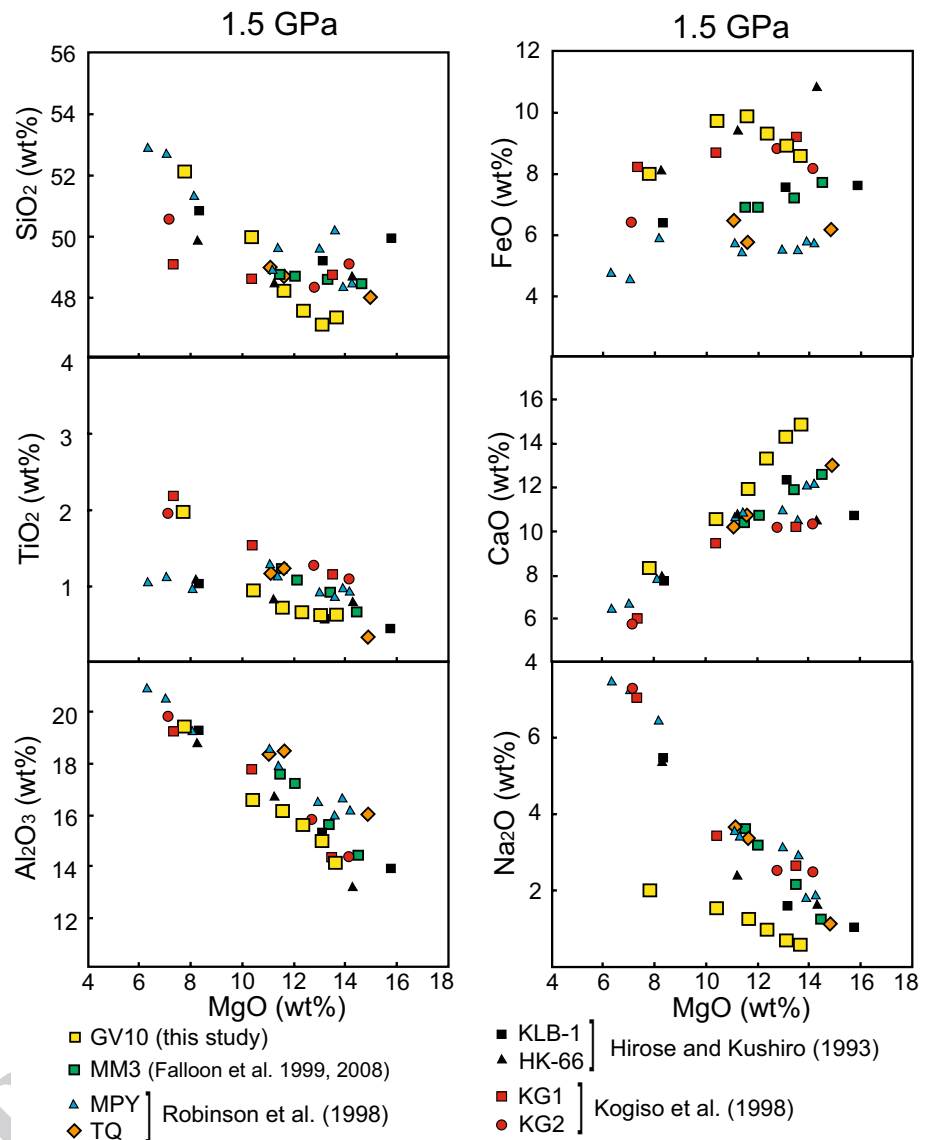
We considered two outermost mantle sources with pyroxenite mass fractions of 5 and 50%. Although the pyroxenite proportion into the mantle is commonly assumed to be around 2–10% (e.g., Hirschmann and Stolper 1996; Pertermann and Hirschmann 2003b), field evidence from orogenic and ophiolitic massifs indicates that the extent of pyroxenites in mantle sequences might be locally significantly higher than 10% (e.g., Gysi et al. 2011). This is for example the case of some outcrops of the External Liguride mantle sequences, in which secondary pyroxenite abundance can reach a proportional ratio of 1:1 to the associated peridotites (Borghini et al. 2013, 2016).

We first envisaged a mantle upwelling scenario along an adiabat with potential temperature (T_P) lower than 1310 °C. At such temperature and 1.5 GPa, pyroxenite GV10 generates low to moderate melt amounts (up to 6.7 and 10.7% for pyroxenite mass fractions of 50 and 5%, respectively), while lherzolite is at subsolidus or incipient melting conditions. Partial melts from low to moderate degrees of melting of GV10 ($F < 12\%$) are Qz- or Hy-normative (Table 3). Therefore, they are expected to react with adjacent unmolten peridotite, producing orthopyroxene-rich reaction zone, as described for eclogite melts–peridotite interaction (Yaxley and Green 1998; Yaxley 2000; Sobolev et al. 2005, 2007). As the ambient peridotite has zero or near-zero porosity and rather higher solidus temperature, these melts should freeze and crystallize at the pyroxenite–peridotite boundary. If pyroxenite-derived melts are able to percolate and impregnate the adjacent peridotite, they are expected to form orthopyroxene- and clinopyroxene-enriched peridotites (e.g., Lambart et al. 2012). Similar peridotites, refertilized by interaction with pyroxenite-derived melts, have been documented in various natural case studies (e.g., Pearson et al. 1993; Rivalenti et al. 1995; Varfalvy et al. 1996;

Zanetti et al. 1996; Mukasa and Shervais 1999; Bodinier et al. 2004; Borghini et al. 2013).

Along the adiabatic upwelling of such heterogeneous mantle, this metasomatic process is likely to be continuous, as documented by experimental works on peridotite-eclogite reaction (Yaxley and Green 1998; Rosenthal et al. 2014). Multiple events of reaction and freezing processes introduce lithological zonation at the pyroxenite–peridotite boundary. In the case of reaction between silica-rich partial melts and peridotite, the resulting orthopyroxene-rich borders can act as permeability barrier that prevents melt escaping from pyroxenite (e.g., Kogiso et al. 2004b; Rosenthal et al. 2014). If infiltration of melts from pyroxenite into surrounding peridotite is inhibited, large batch of pyroxenitic melts could be retained in equilibrium with solid residues, isolated from further reaction with peridotite (Lambart et al. 2012). Mechanical instabilities caused by melt accumulation can lead to rapid expulsion of these melts into veins or channels (Kogiso et al. 2004b).

Extraction of melt fractions from pyroxenite GV10 would leave a wehrlitic residue made by a clinopyroxene + olivine (±spinel) assemblage, introducing a range of clinopyroxene-rich heterogeneities in the rising mantle. Their bulk compositions, calculated using the compositions of residual minerals in our experiments, are similar to the bulk composition of clinopyroxenites investigated by Kogiso and Hirschmann (2001) (Fig. 5). Such residual components have Mg-rich minerals and low jadeite contents in clinopyroxene, and their solidus temperature can be significantly increased above that of the ambient peridotite (e.g., Rosenthal et al. 2014; Lambart et al. 2016).

For mantle adiabats with potential temperature (T_P) > 1310 °C, along the pressure interval 1–1.5 GPa, pyroxenite and peridotite are melting simultaneously and the melt productivity of the two components will depend on their mass fractions in the source (e.g., Phipps Morgan 2001). To make some inferences on the contribution of secondary pyroxenite GV10 on major element chemistry of basalts, we computed the compositions of melts produced by mixed pyroxenite–peridotite sources at 1 GPa (Fig. 12). We used the pyroxenite and peridotite "instantaneous" melt fractions provided by the isentropic decompression melting model of Lambart et al. (2016), assuming two pyroxenite/peridotite mass fractions in the source as described above (5 and 50% of GV10), and different T_P of the ascending mantle (Suppl. Figure 3). A fundamental assumption of this approach is that pyroxenite and peridotite behave as two closed systems, i.e. in thermal equilibrium but chemically isolated, until melt mixing and extraction, as assumed in previous melting models (e.g., Lambart et al. 2009a; Shortle and Maclennan 2011; Sorbadere et al. 2013). This also implies that partial melts remain in equilibrium with their solid residues until extraction.

Major element compositions of melts used in the calculations were derived from experimental results on pyroxenite GV10 (this study) and lherzolite MM3 (Baker and Stolper 1994; Falloon et al. 2008). This latter resembles the composition of External Liguride lherzolites hosting secondary pyroxenite GV10, which were chemically and isotopically identified as a potential MORB-type mantle source (Rampone et al. 1995; Borghini et al. 2013). For each pyroxenite–peridotite melt fraction pair, obtained at 1 GPa for different T_P using Lambart et al. (2016) modeling, we mixed the composition of pyroxenite GV10 and lherzolite MM3 melts using the method proposed by Sorbadere et al. (2013) (see details in caption of Fig. 12). In Fig. 12, the compositions of mixed melts resulting from this model are plotted together with the compositional field defined by the most primitive MORBs. These latter were selected from a broad database recently compiled by Gale et al. (2013), considering only glass compositions with $X_\mathrm{Mg} \geq 0.67$, i.e. liquids close to equilibrium with mantle olivine. This selection reduced the original dataset of 12,527 compositions to only 184 glass compositions.

The dashed colored lines in Fig. 12 approximate the range of composition of melts generated for different fixed T_P by varying the mass fraction of secondary pyroxenite in the source from 5 to 50%. The increase of secondary pyroxenite GV10 component in the source results in mixed melts with higher FeO, CaO and lower Al_2O_3, Na_2O contents, whereas it only weakly influences the SiO_2 and TiO_2 abundances (Fig. 12). SiO_2 and FeO contents plot far from the composition of px-MORBs (Lambart et al. 2013), and the CaO/Al_2O_3 ratio of mixed melts still varies within the range of MORB (CaO/Al_2O_3 <0.9). MgO contents of mixed melts remain rather constant for low T_P but it tends to significantly decrease, at increasing pyroxenite mass fraction, assuming T_P > 1330 °C (Fig. 12). As expected, at fixed pyroxenite fraction in the source, MgO of mixed melts is positively correlated with T_P, reflecting higher melting degrees of both mantle components (peridotite and secondary pyroxenite).

Melt compositions derived by the model match the variability defined by the most primitive MORB for most of the major element oxides. Melt compositions best fitting the compositional variability of MORBs are those calculated assuming T_P in the range 1280–1370 °C. The major discrepancy is given by the higher X_Mg of mixed melts produced at higher T (>1370 °C), mostly from 5%-pyroxenite source (Fig. 12), which more closely resemble the X_Mg values of peridotite-derived melts. As expected, this mismatch tends to be higher at higher temperature (i.e. at higher melting degrees). However, the X_Mg of melts may be rapidly homogenized to MORB values by early olivine fractionation (e.g., Langmuir et al. 1992), melt-rock reaction within dunite channels (e.g., Kelemen et al. 1995; Asimow and
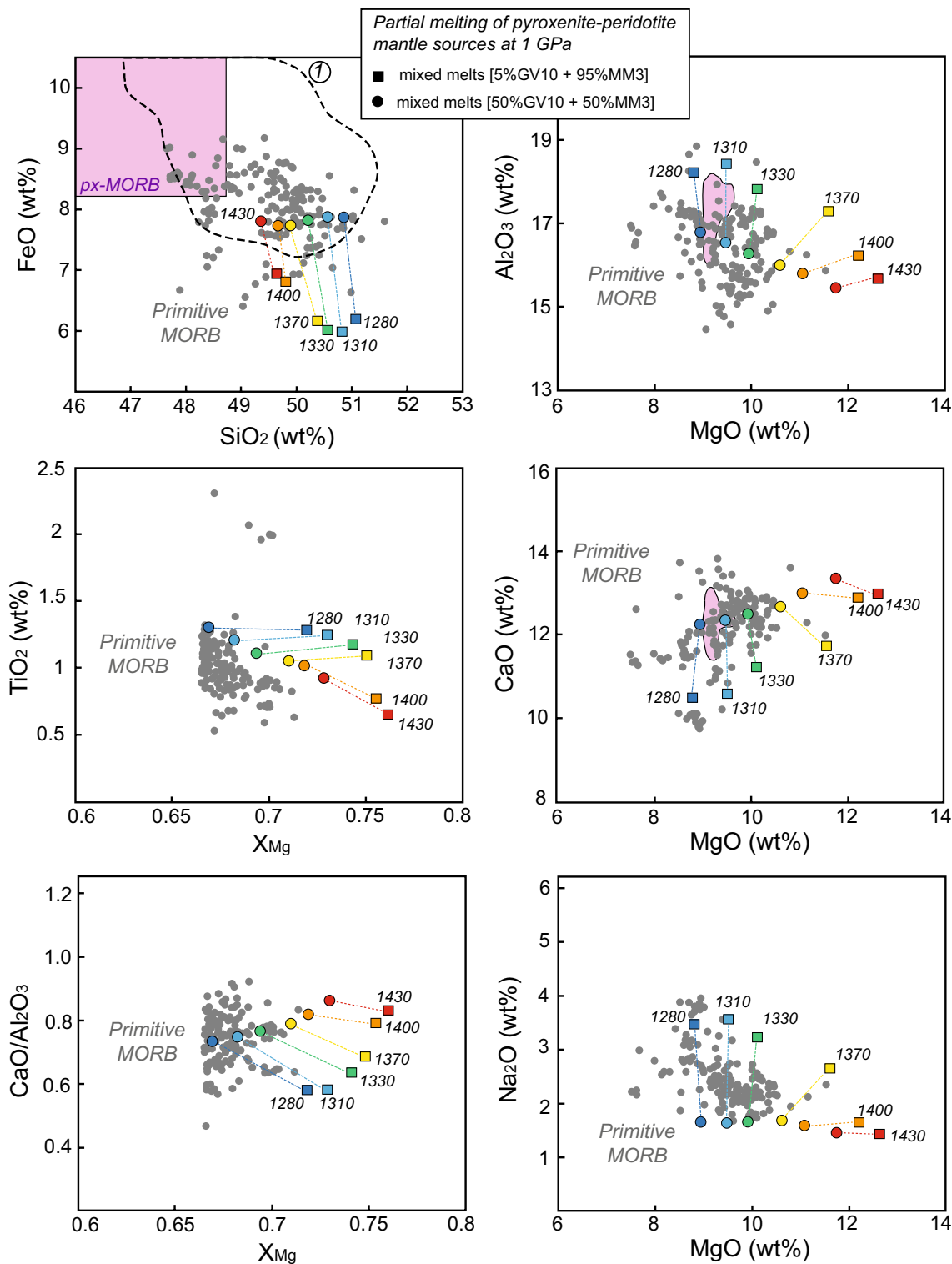
Stolper 1999; Lambart et al. 2009b) and/or reactive crystallization (e.g., Collier and Kelemen 2010). Therefore, the results of our modeling do not allow discriminating the T_P of MORB generation.

To sum up, the results of this model support the postulation that secondary pyroxenite, as the one investigated in this study, potentially represents a hidden component in the MORB mantle source (e.g., Shorttle and Maclennan 2011; Lambart et al. 2013; Rosenthal et al. 2014). A remarkable implication is that, if secondary pyroxenites inherited trace element and/or isotopic enriched signature during their formation by melt-rock reaction processes, their presence in

◄**Fig. 12** SiO$_2$ versus FeO; Al$_2$O$_3$, CaO and Na$_2$O versus MgO; CaO/Al$_2$O$_3$ and TiO$_2$ versus X_{Mg} of partial melts produced by decompression melting of two-lithologies mantle source at 1.0 GPa. Melt compositions resulting from the model are compared to the compositions of the most primitive MORB (with $X_{Mg} \geq 0.67$; Gale et al. 2013). In SiO$_2$ versus FeO diagram, the field "1" (*black dashed line*) represent the compositional variability of MORB with MgO ≥ 9 wt%. *Colored numbers* refer to the potential Temperature (T_P) adopted in the isentropic decompression melting model (Lambart et al. 2016), to derive the "instantaneous" melt fractions produced simultaneously by secondary pyroxenite GV10 and a fertile lherzolite (see Supplementary Figure 3). *Colored dashed lines* represent the approximated trend of melt composition variability from mixed sources with 5 to 50% pyroxenite at a given T_P. For the fertile lherzolite we adopted the solidus temperature parameterization proposed by Hirschmann (2000) (see the text for further explanation). Calculations include two heterogeneous mantle sources made by 5% (secondary pyroxenite) GV10 + 95% (fertile lherzolite) MM3 and 50% GV10 + 50% MM3. We derive the mass fraction of pyroxenite-derived melt in aggregated liquids (LF$_{Py}$) by the equation LF$_{Py}$ = $\Psi \times F_{Py}/[(\Psi \times F_{Py}) + (1 - \Psi) \times F_{Per}]$, where Ψ is the mass fraction of pyroxenite in the source, F_{Py} and F_{Per} are the melt fractions produced by pyroxenite and peridotite, respectively (Lambart et al. 2009a). The composition of aggregated "instantaneous" melts is provided by the equation: $X_{mix} = (X_{Py} \times LF_{Py}) + (X_{Per} \times LF_{Per})$, where X_{mix}, X_{Py} and X_{Per} are the weight percentages of a given element in the aggregated melt, pyroxenite melt and peridotite melt, respectively, and LF$_{Per}$ is the liquid fraction from the peridotite $(1 - LF_{Py})$ (Sorbadere et al. 2013). Melt compositions at the given F have been derived from experiments on GV10 (this study) and MM3 (Falloon et al. 1999, 2008)

the mantle source could explain the decoupling between "enriched" trace element/isotope and "normal" major element compositions sometimes documented in oceanic basalts (e.g., Salters and Dick 2002; le Roux et al. 2002; Paulick et al. 2010; Zhang et al. 2012). In this context, mantle portions made by embedded secondary pyroxenite and fertile lherzolite as documented in ultramafic massifs (e.g., Borghini et al. 2013), eventually delaminated and incorporated into the asthenosphere, could constitute the source of trace element and isotopic enriched signature in MORBs.

Summary and concluding remarks

We have experimentally determined phase relations, melting conditions and melt and minerals compositions of an anhydrous natural olivine-websterite (GV10), representing a secondary-type pyroxenite, at 1 and 1.5 GPa and temperatures from 1180 to 1400 °C. Residual mineral assemblages are dominated by clinopyroxene and minor olivine (and spinel). Relatively high X_{Mg} and low alkali content of our starting composition result in solidus temperature only slightly lower than fertile lherzolite. At both pressure conditions, higher modal orthopyroxene relative to clinopyroxene is involved in the melting reaction, thus resulting in the early disappearance of orthopyroxene, and high SiO$_2$ contents in melts produced by low- to moderate-melting

degree ($F < 13\%$). Although for many oxides the compositions of partial melts from secondary pyroxenite GV10 are quite similar to those of melts produced by variably fertile lherzolites, they differ for higher CaO contents, resulting in slightly higher CaO/Al$_2$O$_3$ ratios, and very low Na$_2$O abundances. These latter reflect relatively high partition coefficient of Na between residual clinopyroxene and partial melt, together with the low initial bulk content. $D_{Na_2O}^{cpx/liquid}$ values obtained in this study, together with other experimental, define a positive correlation with pressure and temperature.

Profiting by the recent parameterization of Lambart et al. (2016), we have simulated the partial melting of mixed pyroxenite–peridotite sources in the context of adiabatic mantle upwelling. At relatively low potential temperatures ($T_P < 1310$ °C), low fractions of secondary pyroxenite melts are expected to react and freeze within the subsolidus adjacent peridotite, resulting in orthopyroxene-rich reaction zones (or refertilized peridotite) and high-X_{Mg} clinopyroxene-rich residues. At higher T_P, secondary pyroxenite and peridotite melt simultaneously. Melt compositions computed by varying the pyroxenite mass fractions in the source (5–50%) largely encompass the chemical variability defined by most primitive MORBs (mostly in the T_P range 1280–1370 °C), supporting the idea that secondary pyroxenites potentially represent a hidden component in MOR mantle sources. Therefore, fertile mantle peridotite veined by secondary pyroxenite may act as a carrier of trace element and isotopic enriched signature in MORBs.

References

Allègre CJ, Turcotte DL (1986) Implications of a two-component marble-cake mantle. Nature 323:123–127

Asimow PD, Stolper EM (1999) Steady-state mantle-melt interactions in one dimension: equilibrium, transport and melt focusing. J Petrol 40:475–494

Asimow PD, Hirschmann MM, Stolper EM (2001) Calculation of peridotite partial melting from thermodynamic models of minerals and melts, IV. Adiabatic decompression and the composition and mean properties of mid-ocean ridge basalts. J Petrol 42:963–998

Baker MB, Stolper EM (1994) Determining the composition of high-pressure mantle melts using diamond aggregates. Geochim Cosmochim Acta 58:2811–2827

Journal : **Large 410**	Dispatch : **3-7-2017**	Pages : **24**
Article No : **1387**	☐ LE	☐ TYPESET
MS Code : **CTMP-D-17-00017**	☑ CP	☑ DISK

Author Proof

Baker MB, Hirschmann MM, Ghiorso MS, Stolper EM (1995) Compositions of near-solidus peridotite melts from experiments and thermodynamic calculations. Nature 375:308–311

Blundy JD, Falloon TJ, Wood BJ, Dalton JA (1995) Sodium partitioning between clinopyroxene and silicate melts. J Geophys Res 100:15501–15515

Bodinier JL, Menzies MA, Shimizu N, Frey FA, McPherson E (2004) Silicate, hydrous and carbonate metasomatism at Lherz, France: contemporaneous derivatives of silicate melt-harzburgite reaction. J Petrol 45:299–320

Bodinier J-L, Garrido CJ, Chanefo I, Bruguier O, Gervilla F (2008) Origin of pyroxenite-peridotite veined mantle by refertilization reactions: evidence from the Ronda peridotite (Southern Spain). J Petrol 49:999–1025

Borghini G, Fumagalli P, Rampone E (2010) The stability of plagioclase in the upper mantle: subsolidus experiments on fertile and depleted lherzolite. J Petrol 51:229–254

Borghini G, Rampone E, Zanetti A, Class C, Cipriani A, Hofmann AW, Goldstein S (2013) Meter-scale Nd isotopic heterogeneity in pyroxenite-bearing Ligurian peridotites encompasses global-scale upper mantle variability. Geology 41:1055–1058

Borghini G, Rampone E, Zanetti A, Class C, Cipriani A, Hofmann AW, Goldstein S (2016) Pyroxenite layersin the Northern Apennines upper mantle (Italy)—generation by pyroxenite melting and melt infiltration. J Petrol. doi:10.1093/petrology/egv074

Brown EL, Lesher CE (2016) REEBOX PRO: a forward model simulating melting of thermally and lithologically variable upwelling mantle. Geochem Geophys Geosyst 17:3929–3968. doi:10.1002/2016GC006579

Collier ML, Kelemen PB (2010) The case for reactive crystallization at mid-ocean ridges. J Petrol 51:1913–1940

Dasgupta R, Hirschmann MM (2007) A modified iterative sandwich method for determination of near-solidus partial melt compositions. II. Application to determination of near-solidus melt compositions of carbonated peridotite. Contrib Mineral Petrol 154:647–661

Delavault H, Chauvel C, Sobolev A, Batanova V (2015) Combined petrological, geochemical and isotopic modeling of a plume source: example of Gambier Island, Pitcairn chain. Earth Planet Sci Lett 426:23–35

Falloon TJ, Green DH, Danyushevsky LV, Faul UH (1999) Peridotite melting at 1.0 and 1.5 GPa: an experimental evaluation of techniques using diamond aggregates and mineral mixes for determination of near-solidus melts. J Petrol 40:1343–1375

Falloon TJ, Green DH, Danyushevsky LV, McNeill AW (2008) The composition of near-solidus partial melts of fertile peridotite at 1 and 1.5 GPa, implications for the petrogenesis of MORB. J Petrol 49:591–616

Gale A, Dalton CA, Langmuir CH, Su Y, Schilling J-G (2013) The mean composition of ocean ridge basalts. Geochem Geophys Geosyst 14:489–518

Garrido CJ, Bodinier J-L (1999) Diversity of mafic rocks in the Ronda peridotite: evidence for pervasive melt–rock reaction during heating of subcontinental lithosphere by upwelling asthenosphere. J Petrol 40:729–754

Green DH, Falloon TJ (1998) Pyrolite: a ringwood concept and its current expression. In: Jackson I (ed) The earth's mantle. Cambridge University Press, Cambridge, pp 311–378

Green DH, Falloon TJ, Eggins SM, Yaxley GM (2001) Primary magmas and mantle temperatures. Eur J Mineral 13:437–451

Guerenko AA, Geldmacher J, Hoernle KA, Sobolev AV (2013) A composite, isotopically-depleted peridotite and enriched pyroxenite source for Madeira magmas: insights from olivine. Lithos 170–171:224–238

Gysi AP, Jagoutz O, Schmidt MW, Targuisti K (2011) Petrogenesis of pyroxenites and melt infiltrations in the ultramafic complex of Beni Boussera, Northern Morocco. J Petrol 52:1676–1735

Herzberg C (2006) Petrology and thermal structure of the Hawaiian plume from Mauna Kea volcano. Nature 444:605–609

Herzberg C (2011) Identification of source lithology in the Hawaiian and Canary Islands: implications for origins. J Petrol 52:113–146

Herzberg C, Asimow PD (2008) Petrology of some oceanic island basalts: PRIMELT2.XLS software for primary magma calculation. Geochem Geophys Geosyst 8:Q09001. doi:10.1029/2008GC002057

Herzberg C, Asimow PD, Arndr N, Niu Y, Lesher CM, Fitton JG, Cheadle MJ, Saunders AD (2003) Temperature in ambient mantle and plumes: constraints from basalts, picrites and komatiites. Geochem Geophys Geosyst 8. doi:10.1029/2006GC001390

Hirose K, Kushiro I (1993) Partial melting of dry peridotites at high pressures: determination of compositions of melts segregated from peridotite using aggregates of diamond. Earth Planet Sci Lett 114:477–489

Hirschmann MM (2000) Mantle solidus: Experimental constraints and the effects of peridotite composition. Geochem Geophys Geosyst 1(10):1042. doi:10.1029/2000GC000070

Hirschmann MM, Stolper EM (1996) A possible role for garnet pyroxenite in the origin of the 'garnet signature' in MORB. Contrib Mineral Petrol 124:185–208

Hirschmann MM, Asimow PD, Ghiorso MS, Stolper EM (1999) Calculation of peridotite partial melting from thermodynamic models of minerals and melts. III. Controls on isobaric melt production and the effect of water on melt production. J Petrol 40:831–851

Hirschmann MM, Kogiso T, Baker MB, Stolper EM (2003) Alkalic magmas generated by partial melting of garnet pyroxenite. Geology 31:481–484

Hofmann AW (2007) Sampling mantle heterogeneity through oceanic basalts: isotopes and trace elements. In: Carlson RW, Holland HD, Turekian KK (eds) Treatise on Geochemistry, the mantle and core, vol 2. Elsevier, Oxford, pp 61–101

Jackson MG, Dasgupta R (2008) Composition of HIMU, EM1, and EM2 from global trends between radiogenic isotopes and major elements in ocean island basalts. Earth Planet Sci Lett 276:175–186

Kelemen PB, Shimizu N, Salters VJM (1995) Extraction of mid-ocean ridge basalt from the upwelling mantle by focused flow of melt in dunite channels. Nature 375:747–753

Keshav S, Gudfinnsson GH, Sen G, Fei Y (2004) High-pressure melting experiments on garnet clinopyroxenite and the alkalic to tholeiitic transition in ocean-island basalts. Earth Planet Sci Lett 223:365–379

Kinzler RJ (1997) Melting of mantle peridotite at pressures approaching the spinel to garnet transition: application to mid-ocean ridge basalt petrogenesis. J Geophys Res 102:853–874

Kogiso T, Hirschmann MM (2001) Experimental study of clinopyroxenite partial melting and the origin of ultra-calcic melt inclusions. Contrib Mineral Petrol 142:347–360

Kogiso T, Hirschmann MM (2006) Partial melting experiments of bimineralic eclogite and the role of recycled mafic oceanic crust in the genesis of ocean island basalts. Earth Planet Sci Lett 249:188–199

Kogiso T, Hirose K, Takahashi E (1998) Melting experiments on homogeneous mixtures of peridotite and basalt: application to the genesis of ocean island basalts. Earth Planet Sci Lett 162:45–61

Kogiso T, Hirschmann MM, Pertermann M (2004a) High-pressure partial melting of mafic lithologies in the mantle. J Petrol 45:2407–2422

Kogiso T, Hirschmann MM, Reiners W (2004b) Length scales of mantle heterogeneities and their relationship to ocean island basalt geochemistry. Geochim Cosmochim Acta 68:345–360

Lambart S, Laporte D, Schiano P (2009a) An experimental study of pyroxenite partial melts at 1 and 1.5 GPa: implications for the major-element composition of mid-ocean ridge basalts. Earth Planet Sci Lett 288:335–347

Lambart S, Laporte D, Schiano P (2009b) An experimental study of focused magma transport and basalt-peridotite interactions beneath mid-ocean ridges: implications for the generation of primitive MORB compositions. Contrib Mineral Petrol 157:429–451

Lambart S, Laporte D, Provost A, Schiano P (2012) Fate of pyroxenite-derived melts in the peridotitic mantle: thermodynamic and experimental constraints. J Petrol 53:451–476

Lambart S, Laporte D, Schiano P (2013) Markers of the pyroxenite contribution in the major-element compositions of oceanic basalts: Review of the experimental constraints. Lithos 160–161:14–36

Lambart S, Baker MB, Stolper EM (2016) The role of pyroxenite in basalt genesis: Melt-PX, a melting parameterization for mantle pyroxenites between 0.9 and 5 GPa. J Geophys Res 121:5708–5735

Langmuir CH, Klein EM, Plank T (1992) Petrological systematics of mid-ocean ridge basalts: constraints on melt generation beneath ocean ridges. Am Geophys Un Monogr 71:183–280

Laporte D, Toplis M, Seyler M, Devidal JL (2004) A new experimental technique for extracting liquids from peridotite at very low degrees of melting: application to partial melting of depleted peridotite. Contrib Mineral Petrol 146:463–484

Le Roux PJ, Le Roex AP, Schilling J-G, Shimizu N, Perkins WW, Pearce NJG (2002) Mantle heterogeneity beneath the southern Mid-Atlantic Ridge: trace element evidence for contamination of ambient asthenospheric mantle. Earth Planet Sci Lett 203:479–498

Libourel G (1999) Systematics of calcium partitioning between olivine and silicate melt: implications for melt structure and calcium content of magmatic olivines. Contrib Mineral Petrol 136:63–80

Mallik A, Dasgupta R (2012) Reaction between MORB-eclogite derived melts and fertile peridotite and generation of ocean island basalts. Earth Planet Sci Lett 329–330:97–108

Mallik A, Dasgupta R (2013) Reactive infiltration of MORB-eclogite-derived carbonated silicate melt into fertile peridotite at 3 GPa and genesis of alkali magmas. J Petrol 54:2267–2300

Mallik A, Dasgupta R (2014) Effect of variable CO_2 on eclogite-derived andesite and lherzolite reaction at 3 GPa—Implications for mantle source characteristics of alkali ocean island basalts. Geochem Geophys Geosyst 15:1533–1557

Marchesi C, Garrido CJ, Bosch D, Bodinier J-L, Gervilla F, Hidas K (2013) Mantle refertilization by melts of crustal-derived garnet pyroxenite: evidence from the Ronda peridotite massif, southern Spain. Earth Planet Sci Lett 362:66–75

Médard E, Schmidt MW, Schiano P, Ottolini L (2006) Melting of amphibole-bearing wehrlites: an experimental study on the origin of ultra-calcic nepheline-normative melts. J Petrol 47:481–504

Médard E, McCammon CA, Barr JA, Grove TL (2008) Oxygen fugacity, temperature reproducibility, and H_2O contents of nominally anhydrous piston-cylinder experiments using graphite capsules. Am Mineral 93:1838–1844

Montanini A, Tribuzio R (2015) Evolution of recycled crust within the mantle: constraints from the garnet pyroxenites of the External Ligurian ophiolites (northern Apennines, Italy). Geology 43:911–914

Mukasa SB, Shervais JW (1999) Growth of sub-continental lithosphere: evidence from repeated injections in the Balmuccia lherzolite massif, Italian Alps. Lithos 48:287–316

O'Hara MJ (1972) Data reduction and projection schemes for complex compositions. In: EaM U (ed) Progress in experimental petrology. NERC, Manchester, pp 103–126

Paulick H, Mueker C, Schluth S (2010) The influence of small-scale mantle heterogeneities on Mid-Ocean Ridge volcanism: Evidence from the southern Mid-Atlantic Ridge (7 degrees 30'S to 11 degrees 30'S) and Ascension Island. Earth Planet Sci Lett 296:299–310

Pearson DG, Davies GR, Nixon PH (1993) Geochemical constraints on the petrogenesis of diamond facies pyroxenites from the Beni Bousera peridotite massif, North Morocco. J Petrol 34:125–172

Pertermann M, Hirschmann MM (2003a) Anhydrous partial melting experiments on MORB-like eclogite: phase relations, phase compositions and mineral–melt partitioning of major elements at 2–3 GPa. J Petrol 44:2173–2201

Pertermann M, Hirschmann MM (2003b) Partial melting on a MORB-like pyroxenite between 2 and 3 GPa: Constraints on the presence of pyroxenite in basalt source regions from solidus location and melting rate. J Geophys Res 108(B2):2125

Phipps Morgan J (2001) Thermodynamics of pressure release melting of a veined plum pudding mantle. Geochem Geophys Geosyst 2:2000GC000049

Pickering-Witter J, Johnson AD (2000) The effects of variable bulk composition on the melting systematics of fertile peridotitic assemblages. Contrib Mineral Petrol 140:190–211

Pilet S, Baker MB, Stolper EM (2008) Metasomatized lithosphere and the origin of alkaline lavas. Science 320:916

Presnall DC, Gudfinnsson GH, Walter MJ (2002) Generation of mid-ocean ridge basalts at pressures from 1 to 7 GPa. Geochim Cosmochim Acta 66:2073–2090

Prytulak J, Elliot T (2007) TiO_2 enrichment in ocean island basalts. Earth Planet Sci Lett 263:388–403

Rampone E, Hofmann AW, Piccardo GB, Vannucci R, Bottazzi P, Ottolini L (1995) Petrology, mineral and isotope geochemistry of the External Liguride peridotites (Northern Apennines, Italy). J Petrol 123:61–76

Rivalenti G, Mazzucchelli M, Vannucci R, Hofmann AW, Ottolini L, Obermiller W (1995) The relationship between websterite and peridotite in the Balmuccia peridotite massif (NW Italy) as revealed by trace element variations in clinopyroxene. Contrib Mineral Petrol 121:275–288

Robinson JAC, Wood BJ, Blundy JD (1998) The beginning of melting of fertile and depleted peridotite at 1.5 GPa. Earth Planet Sci Lett 155:97–111

Rosenthal A, Yaxley GM, Green DH, Hermann J, Kovacs I, Spandler C (2014) Continuous eclogite melting and variable refertilization in upwelling heterogeneous mantle. Sci Rep 4:6099

Salters VJM, Dick HJB (2002) Mineralogy of the mid-ocean-ridge basalt source from neodymium isotopic composition of abyssal peridotites. Nature 418:68–72

Schwab B, Johnston A (2001) Melting systematics of modally variable, compositionally intermediate peridotites and the effects of mineral fertility. J Petrol 42:1789–1811

Shen Y, Forsyth DW (1995) Geochemical constraints on initial and final depths of melting beneath mid-ocean ridges. J Geophys Res 100:2211–2237

Shorttle O, Maclennan J (2011) Compositional trends of Icelandic basalts: implications for short-length scale lithological heterogeneity in mantle plumes. Geochem Geophys Geosyst 12:Q11008

Shorttle O, Maclennan J, Lambart S (2014) Quantifying lithological variability in the mantle. Earth Planet Sci Lett 395:24–40

Sobolev AV, Hofmann AW, Sobolev SV, Nikogosian IK (2005) An olivine-free mantle source of Hawaiian shield basalts. Nature 434:590–597

Sobolev AV, Hofmann AW, Kuzmin DV, Yaxley GM, Arndt NT, Chung S-L, Danyushevsky LV, Elliott T, Frey FA, Garcia MO, Gurenko AA, Kamenetsky VS, Kerr AC, Krivolutskaya NA, Matvienkov VV, Nikogosian IK, Rocholl A, Sigurdsson IA, Sushchevskaya NM, Teklay M (2007) The amount of recycled crust in sources of mantle-derived melts. Science 316:412–417

Sorbadere F, Medard E, Laporte D, Schiano P (2013) Experimental melting of hydrous peridotite-pyroxenite mixed sources: constraints on the genesis of silica-undersaturated magmas beneath volcanic arcs. Earth Planet Sci Lett 384:42–56

Spandler C, Yaxley GM, Green DH, Rosenthal A (2008) Phase relations and melting of anhydrous K-bearing eclogite from 1200 to 1600°C and 3 to 5 GPa. J Petrol 49:771–795

Stracke A, Bourdon B (2009) The importance of melt extraction for tracing mantle heterogeneity. Geochim Cosmochim Acta 73:218–238

Toplis MJ (2005) The thermodynamics of iron and magnesium partitioning between olivine and liquid: criteria for assessing and predicting equilibrium in natural and experimental systems. Contrib Mineral Petrol 149:22–39

Ulmer P, Luth RW (1991) The graphite fluid equilibrium in P, T, fO2 space: an experimental determination to 30 kbar and 1600°C. Contrib Mineral Petrol 106:265–272

Varfalvy V, Herbert R, Bedard JH (1996) Interactions between melt and upper-mantle peridotites in the North Arm Mountain Massif, Bay of Islands Ophiolite, Newfoundland, Canada: implications for the genesis of boninites and related magmas. Chem Geol 129:71–90

Villiger S, Ulmer P, Müntener O (2007) Equilibrium and fractional crystallization experiments at 0.7 GPa; the effect of pressure on phase relations and liquid compositions of tholeiitic magmas. J Petrol 48:159–184

Walter MJ (1998) Melting of garnet peridotite and the origin of komatiite and depleted lithosphere. J Petrol 39:29–60

Wasylenki LE, Baker MB, Kent AJR, Stolper EM (2003) Near-solidus melting of the shallow upper mantle: partial melting experiments on depleted peridotite. J Petrol 44:1163–1191

Yasuda A, Fujii T, Kurita K (1994) Melting phase relations of an anhydrous mid-ocean ridge basalt from 3 to 20 GPa: implications for the behavior of subducted oceanic crust in the mantle. J Geophys Res 99:9401–9414

Yaxley GM (2000) Experimental study of the phase and melting relations of homogeneous basalt + peridotite mixtures and implications for the petrogenesis of flood basalts. Contrib Mineral Petrol 139:326–338

Yaxley GM, Green DH (1998) Reactions between eclogite and peridotite: mantle refertilisation by subduction of oceanic crust. Schweiz Mineral Petrogr Mitt 78:243–255

Yaxley GM, Sobolev AV (2007) High-pressure partial melting of gabbro and its role in the Hawaiian magma source. Contrib Mineral Petrol 154:371–383

Zanetti A, Vannucci R, Bottazzi P, Oberti R, Ottolini L (1996) Infiltration metasomatism at Lherz as monitored by systematic ion-microprobe investigations close to a hornblendite vein. Chem Geol 134:113–133

Zhang GL, Zong CL, Yin XB et al (2012) Geochemical constraints on a mixed pyroxenite-peridotite source fro East Pacific Rise basalts. Chem Geol 330:176–187

🐎 **Springer**

the language of science

Author Query Form

Please ensure you fill out your response to the queries raised below and return this form along with your corrections

Dear Author

During the process of typesetting your article, the following queries have arisen. Please check your typeset proof carefully against the queries listed below and mark the necessary changes either directly on the proof/online grid or in the 'Author's response' area provided below

Query	Details Required	Author's Response
AQ1	Please check the clarity of the sentence 'Profiting of available experimental data, increasingly sophisticated geochemical models have investigated the role of mixed pyroxenite-peridotite mantle sources in the genesis of mid-ocean ridge basalts.'	
AQ2	Reference: References [Gysi et al. (2012), Lambart et al. (2009)] was mentioned in the manuscript; however, this was not included in the reference list. As a rule, all mentioned references should be present in the reference list. Please provide the reference details to be inserted in the reference list.	
AQ3	Kindly check and confirm layout of Table 3, amend if necessary.	
AQ4	Kindly check and confirm reference Pickering and Johnson (2000) has been changed to Pickering-Witter and Johnson (2000) so that this citation matches the list.	
AQ5	Kindly provide page range of reference Herzberg et al. (2003).	
AQ6	Kindly check and confirm processed article title of reference Lambart et al. (2009a).	

Author Proof